Bounded-strength dynamical control of a qubit based on Eulerian cycles

A Thesis

Submitted to the faculty

in partial fulfillment of the requirements for the

Degree of Master of Science in Physics

by

S. Taylor Smith

DARTMOUTH COLLEGE

Hanover, NH

October 2007

Lorenza Viola, Advisor

Walter E. Lawrence

Miles Blencowe

Abstract

Decoherence and faulty quantum control are two of the biggest obstacles to realizing a scalable quantum information processing device, among a number of other exciting applications utilizing the unique properties of quantum systems. Here we review the original work on both bang-bang and Eulerian dynamical decoupling, designed to beat decoherence in open quantum systems, and investigate the performance of each in a simple but instructive control setting. In particular, we consider the limit of low-power control and the effect of two types of systematic errors in control implementation. We find that sequences designed to work with bang-bang pulses perform quite poorly with bounded-strength control, and that performance is recovered by using the Eulerian method. The structure of this method is based on Eulerian cycles on the Cayley graph of a decoupling group, and is explicitly designed to work with bounded-strength control. A time-symmetrized Eulerian sequence proves particularly robust to changes in control strength. Adding systematic control errors, we investigate predictions of the fault-tolerant properties of the Eulerian method, finding again that a time-symmetrized Eulerian sequence emerges as a promising new option for fault-tolerant decoherence control.

Acknowledgements

I would like to thank my advisor, Lorenza Viola, for everything she has taught me, both in physics and in what it means to be a physics student, and Lea Dos Santos, for wonderful explanations and support in difficult times.

Contents

Chapter 1

Introduction and Motivations

Any real quantum system is unavoidably coupled to the surrounding environment, leading to non-unitary, open-system dynamics [1]-[3]. The same may be said of any physical system, but for quantum systems the effects of this coupling are particularly profound, since entanglement with environmental degrees of freedom leads to decoherence and the loss of uniquely quantum capabilities. For the many exciting applications which seek to make use of the coherences in quantum states, understanding how to control the process of decoherence is of vital importance. For example, finding a way to maintain these coherences over the timescales required remains one of the biggest obstacles for realizing scalable quantum information processing devices [4]-[8]. Other applications include quantum state engineering [9], quantum interferometry [10], and high-resolution nuclear [11], [12] and molecular [13] spectroscopy; additionally, designing nanoscale processes or devices to operate properly in the quantum-limited regime will require an understanding of how to maintain coherent quantum behavior in the presence of environmental noise [13], [14].

A number of strategies for decoherence control have emerged in recent years as interest in this field has swelled tremendously. These can generally be divided into passive techniques, such as quantum reservoir engineering [16], decoherence-free subspaces [17]-[19], and noiseless-subsystem encoding [20], including topological approaches [21]-[23]; and active techniques such as quantum feedback control [24]-[28], quantum error-correcting codes [29]-[30], concatenated coding [31], and dynamical decoupling [32]-[42], which are philosophically closer to quantum control theory [43]-[46]. Strategies such as decoherence-free subspaces and error-correcting codes which are based on encoding have the disadvantage of requiring large amounts of ancillary space, contributing to the

scalability problem [47]–an issue which is avoided in both closed-loop control strategies such as quantum feedback control and open-loop control strategies such as dynamical decoupling. Between these, open-loop strategies have the advantage of being simpler and requiring less knowledge of the environmental interaction.

Here we focus on dynamical decoupling, first presented by Viola, Lloyd, and Knill in [33] and [45], and in particular the Eulerian method presented in [42]. Dynamical decoupling (DD) has its conceptual roots in techniques developed for high-resolution nuclear magnetic resonance (NMR) spectroscopy since the advent of the Hahn spin echo experiment [48]. Specifically, it is based on coherent averaging techniques for the removal of unwanted contributions to the nuclear spin Hamiltonian, since the problem of decoherence control can also be phrased in terms of effectively removing system-environment interaction terms from the total Hamiltonian.

The goal of DD, in the context of this investigation, will be to effectively "freeze" the evolution of a system, described by Hamiltonian H_0, by modifying its natural dynamics with a time-dependent control Hamiltonian $H_c(t)$, so that $H(t) = H_0 + H_c(t)$. In order to analyze the controlled dynamics, it is common to move into a frame which "follows" the applied control Hamiltonian, in which explicit reference to the control disappears [11], [12]. This is often called the "logical" or "toggling" frame, and it is similar to the interaction picture which is often used in the case of a system with a time-independent Hamiltonian subject to a time-dependent potential; that is, a frame which rotates with the system Hamiltonian, allowing the time-dependent interaction to be studied independently. In our case, however, the relevant interaction frame follows the time-dependent portion of the total Hamiltonian.

The total propagator in the physical frame, with the control, is given by the time-ordered exponential

$$U(t) = T\exp\left\{-i\int_0^t \left[H_0 + H_c(s)\right] ds\right\}, \tag{1.1}$$

where for simplicity $\hbar$ has been set to 1, as it will be henceforth. The propagator corresponding only to the control Hamiltonian is given by

$$U_c(t) = T\exp\left\{-i\int_0^t H_c(s) ds\right\}. \tag{1.2}$$

Just as in moving to the interaction picture, we can transform operators to the frame which follows $H_c(t)$ by computing $\widetilde{A}(t) = U_c^\dagger(t) A\, U_c(t)$ for any given operator A, where the tilde indicates a

quantity in the logical frame. In particular, $\widetilde{\rho}(t) = U_c^\dagger(t)\widetilde{\rho}(t)U_c(t)$ for the density operator describing the state of the system. Thus, the logical frame Hamiltonian is given by

$$\widetilde{H}_0(t) = U_c^\dagger(t) H_0 \, U_c(t). \tag{1.3}$$

The logical frame propagator corresponding to this Hamiltonian is

$$\widetilde{U}(t) = T\exp\left\{-i\int_0^t \widetilde{H}_0(s)\, ds\right\}, \tag{1.4}$$

which, by exploiting the fact that the two frames coincide at $t = 0$, is related to the physical frame propagator by

$$U(t) = U_c(t)\widetilde{U}(t). \tag{1.5}$$

One of the primary requirements for the control propagator $U_c(t)$ is that it be cyclic, with some period which we will call the cycle time T_c, so that $U_c(nT_c) = \mathbb{I}$, with n an integer. At each time nT_c, the physical frame and logical frame propagators coincide, so if we observe the time evolution stroboscopically, synchronized with the control, the logical frame propagator $\widetilde{U}(t)$ is sufficient to describe the evolution. In order to better understand its effect over one cycle, we turn to so-called average Hamiltonian theory (AHT) [12], [49], [11], in which we seek to express the action of the full time-dependent logical frame Hamiltonian over one cycle,

$$U(T_c) = T\exp\left\{-i\int_0^{T_c} \widetilde{H}_0(s)\, ds\right\}, \tag{1.6}$$

in terms of a time-independent "average" Hamiltonian $\bar{H}_0$, such that

$$U(T_c) = \exp\{-i\bar{H}_0 T_c\}. \tag{1.7}$$

By expanding the exponential in (1.6) as a function of the control parameter T_c and collecting terms of equal order, $\bar{H}_0$ may be rewritten as a power series,

$$\bar{H}_0 = \bar{H}_0^{(0)} + \bar{H}_0^{(1)} + \bar{H}_0^{(2)} + \cdots, \tag{1.8}$$

known as the Magnus expansion [12], where the lowest-order terms have simple explicit expressions:

$$\begin{aligned}
\bar{H}_0^{(0)} &= \frac{1}{T_c}\int_0^{T_c} dt_1 \widetilde{H}_0(t_1), \\
\bar{H}_0^{(1)} &= -\frac{i}{2T_c}\int_0^{T_c} dt_2 \int_0^{t_2} dt_1 \left[\widetilde{H}_0(t_2), \widetilde{H}_0(t_1)\right], \\
\bar{H}_0^{(2)} &= -\frac{1}{6T_c}\int_0^{T_c} dt_3 \int_0^{t_3} dt_2 \int_0^{t_2} dt_1 \Big\{ \left[\widetilde{H}_0(t_3), \left[\widetilde{H}_0(t_2), \widetilde{H}_0(t_1)\right]\right] + \left[\left[\widetilde{H}_0(t_3), \widetilde{H}_0(t_2)\right], \widetilde{H}_0(t_1)\right] \Big\}.
\end{aligned} \tag{1.9}$$

Since our goal is to freeze the evolution of the system, we would like to have the propagator $\widetilde{U}(t)$ yield no net effect at the end of one cycle; that is, we would like to have $\bar{H}_0 = 0$. In practice, since decoupling schemes are built by assuming that only a restricted set of control operations is available for control, achieving $\bar{H}_0 = 0$ need not be possible to all orders. However, since higher-order terms depend on higher powers of T_c, as T_c becomes small these go to zero, and $\bar{H}_0$ is well approximated by the lowest order terms. Thus we seek to get rid of the dominant terms, $\bar{H}_0^{(0)} = 0$ and $\bar{H}_0^{(1)} = 0$, by designing an appropriate control propagator $U_c(t)$.

Insight into designing a control propagator to cancel $\bar{H}_0$ comes from group theory. Given a discrete group $\mathcal{G}$ of order $|\mathcal{G}| > 1$ whose elements have unitary representations acting on the state space of the system, $\{g_0, g_1, g_2, ..., g_L\}$, where $L = |\mathcal{G}| - 1$, there exist two general approaches: the more familiar, by now, "bang-bang" (BB) decoupling, and the Eulerian method of decoupling proposed by Viola and Knill in [42]. In the BB formulation, cancellation of $\bar{H}_0^{(0)}$ is achieved by sequentially realizing the group elements $\{g_0, g_1, g_2, ..., g_L\}$ with the control propagator in successive time intervals $\Delta t = T_c/|\mathcal{G}|$. That is,

$$U_c(t) = \begin{cases} g_0; & t \in [0, \Delta t) \\ g_1; & t \in [\Delta t, 2\Delta t) \\ \vdots & \\ g_L; & t \in [(L-1)\Delta t, L\Delta t) \end{cases} \tag{1.10}$$

This means that at the end of every time interval $l\Delta t$, the control propagator changes instantaneously from g_{l-1} to $g_l = (g_l g_{l-1}^\dagger) g_{l-1}$ by the application of the unitary control "pulse" $p_l = g_l g_{l-1}^\dagger$; in practice, for our system, a rotation of the spin through a finite angle. Although theoretically effective, this method has the disadvantage of being fundamentally unrealizable, because true implementation

of such an instantaneous but finite rotation would require a control Hamiltonian infinite in amplitude and applied for an infinitely short time. Furthermore, even when an approximation of BB pulses is used, which occurs frequently in NMR spectroscopy research, the application of high-power control fields may be problematic, most importantly because of the poor frequency selectivity associated with narrow pulses. Minimizing the required control amplitudes is thus important for realistic DD applications.

The idea of the Eulerian method is to remove the need for instantaneous control operators by using a bounded-strength Hamiltonian to steer the control propagator smoothly from one group element to the next over a finite time period Δt, rather than the discrete "jumps" of BB decoupling– for examples of other work in this area see [50] and [51]. This approach is called Eulerian because in order to cancel $\bar{H}_0^{(0)}$, the path of the control propagator must realize an "Eulerian cycle" on the Cayley graph of the decoupling group. The Cayley graph is constructed by labeling vertices with the elements of $\mathcal{G}$ and connecting them with directed edges, which are "colored" with elements in the generating set of $\mathcal{G}$. Let $\Gamma = \{\gamma_\lambda\}$ be the generating set, with $\lambda = 0, 1, ..., |\Gamma| - 1$. Then the directed edge from g_{l-1} to g_l is colored with the generator γ_λ if and only if $g_l = \gamma_\lambda g_{l-1}$. An Eulerian cycle is defined as a cycle which traverses each edge exactly once; since Cayley graphs are regular–that is, each vertex has the same degree–it is guaranteed that an Eulerian cycle will exist [52].

The cycle can be defined by a sequence of colors starting at the identity element g_0 of $\mathcal{G}$: $C_E = (c_1, c_2, ..., c_l)$, where $c_l = \gamma_\lambda$ for some λ. This determines a well-defined path, because each vertex has exactly one departing edge of each color. The Eulerian control formulation then consists of "traversing" the edges indicated by C_E, where "traversing" means that instead of jumping instantaneously from one vertex (group element) to the next, as in the BB case, the control is guided continuously from one group element to the next by a finite control Hamiltonian, *i.e.* such that the appropriate generator (pulse) is realized at the end of the time interval Δt, so we have

$$\gamma_\lambda = T \exp\left\{-i \int_0^{\Delta t} h_\lambda(s)\, ds\right\} \tag{1.11}$$

for some choice of a (possibly time-dependent) Hamiltonian h_λ. Since the group may have multiple generators, this approach may lengthen the cycle time; if the group has γ generators, the Eulerian cycle time is $\gamma|\mathcal{G}|$, compared to $|\mathcal{G}|$ for the instantaneous scheme. However, it should be noted that this is only a polynomial overhead. Because the choice of h_λ is arbitrary we can also imagine schemes

in which it differs from zero only over some portion of the control interval Δt; in particular, h_λ may be piecewise constant in various unequivalent ways.

In addition to being more physically realistic and causing less unwanted disturbance in the target system, the Eulerian method has been predicted in [42] to be more robust to systematic control errors. This is quite a significant property; above we mentioned that decoherence is one of the biggest obstacles to realizing a scalable quantum computer—the other is inevitably faulty quantum controls. To this end, much work has been done to come up with fault-tolerant control schemes, see [53]-[60] for examples. The Eulerian method has the advantage that, in the case where each h_λ is always associated with a characteristic error, it guarantees that we will still have $\bar{H}_0^{(0)} = 0$. We will examine this in Chapter 4. In Chapter 2 we consider ideal control in the simplest dynamical decoupling setting, in which the BB and Eulerian sequences happen to coincide; in Chapter 3 we will examine a more general setting and will see the effect of naively transcribing a BB sequence for use with finite pulses and the contrast with Eulerian control.

Chapter 2

Control of Known Single-Qubit Dynamics

The simplest dynamical decoupling scenario we can think of is that of a single qubit subject to a known constant Hamiltonian. Without loss of generality, we can think of this as a spin in a constant magnetic field whose direction is known. Labeling this the z direction, the system is described by a Hamiltonian $H_0 = B_z\sigma_z$. If the two qubit states are denoted $|0\rangle$ and $|1\rangle$, with energies E_0 and E_1, respectively, where $E_1 > E_0$, the quantity B_z representing the magnetic field is defined as $B_z \equiv (E_1 - E_0)/2$, and $\sigma_z = |1\rangle\langle 1| - |0\rangle\langle 0|$. Please note that everywhere in this discussion we will take $\hbar = 1$. Thus, the propagator for the system is given by

$$\begin{aligned} U(t-t_0) &= \exp\{-iB_z\sigma_z(t-t_0)\} \\ &= \cos[B_z(t-t_0)]\,\mathbb{I} - i\sin[B_z(t-t_0)]\,\sigma_z \end{aligned} \tag{2.1}$$

which returns to the identity after a period of $T = 2\pi/B_z$ or, up to a phase, after $T = \pi/B_z$. That is, in the absence of control the spin simply precesses around the z-axis with a timescale determined by B_z. This periodic return to the original state is not, in general, a characteristic of more complicated systems; we will return to the significance of this feature later. Both because and in spite of this system's simplicity, it is useful for illustrating the machinery of dynamical decoupling, in preparation for more complicated control settings.

2.1 Bang-bang decoupling

As mentioned above, the free evolution of this system already achieves the desired result of no net evolution if we sample it stroboscopically at times $t_n = nT$. However, we seek to remove the evolution due to H_0 on a controllable timescale T_c. A pulse sequence to achieve this need only consist of rotations around x or y–here we will use x, corresponding to the decoupling group $\mathcal{G} = \{\mathbb{I}, \sigma_x\}$. Physically, one can think of allowing the qubit to evolve for some time Δt, in which the spin precesses about z, rotating the spin about the x-axis with a π_x pulse, allowing the qubit again to evolve for Δt, and applying another π_x pulse, returning the spin perfectly to its original position after $t = 2\Delta t$. Diagrams such as this are useful for visualizing the pulse sequence:

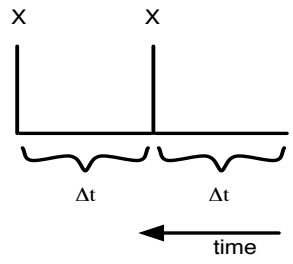

Please note that the forward time direction in all such diagrams will be to the left, to make the analogy with operator ordering clearer. The propagator describing this cycle in the physical frame is

$$U(2\Delta t) = P_2\, e^{-iH_0\Delta t} P_1\, e^{-iH_0\Delta t},$$

where $e^{-iH_0\Delta t}$ represents the interval of free evolution, and the propagator for a pulse—a π_x rotation—is given by

$$P_1 = P_2 = e^{-i\pi\sigma_x/2}.$$

Just by carrying out this multiplication we can see that $U(2\Delta t) = \mathbb{I}$, up to a phase factor. However, we can see also see this in another way by applying the group-theoretic formalism that will be useful for more complicated cases.

Recall that the BB dynamical decoupling prescription, given a decoupling group $\mathcal{G}$, is to sequentially realize with the control propagator the representations of the elements of $\mathcal{G}$, as in (1.10). Thus, appropriately for our decoupling group $\mathcal{G} = \{\mathbb{I}, \sigma_x\}$, the control propagator $U_c(t) = T\exp\left\{-i\int_0^t H_c(s)ds\right\}$

over the cycle is

$$U_c(t) = \begin{cases} \mathbb{I} & 0 \leq t < \Delta t \\ \sigma_x & \Delta t \leq t < 2\Delta t \end{cases} \tag{2.2}$$

remembering that $P_1 = \exp\{-i\pi\sigma_x/2\} = \sigma_x$ up to a phase factor. The control propagator "builds up" over time; at each time it includes (in time-ordered fashion), all control which has taken place so far. In the first interval, $t \in [0, \Delta t)$, $U_c = \mathbb{I}$ because no control actions have taken place yet; at $t = \Delta t$, the pulse P_1 is implemented instantaneously, so in the next interval $U_c = P_1 = \sigma_x$. At $t = 2\Delta t$ there is another pulse, so $U_c(2\Delta t) = P_2 P_1 = \mathbb{I}$, up to a phase factor, to complete the cycle.

Taking the original Hamiltonian in the logical frame corresponding to this control propagator,

$$\widetilde{H}_0(t) = U_c^\dagger(t) H_0 U_c(t),$$

we want to compute the first terms in the average Hamiltonian over the cycle period $2\Delta t$ with the control scheme we have selected. Recalling the form of the terms in the Magnus expansion (1.9), the zeroth order contribution to the average Hamiltonian is

$$\begin{aligned} \bar{H}_0^{(0)} &= \frac{1}{2\Delta t}\int_0^{2\Delta t} U_c^\dagger(t_1) H_0 U_c(t_1) dt_1 \\ &= \frac{1}{2\Delta t}\left[\int_0^{\Delta t} \mathbb{I} H_0 \mathbb{I}\, dt_1 + \int_{\Delta t}^{2\Delta t} \sigma_x H_0 \sigma_x dt_1\right] \\ &= \frac{1}{2\Delta t}\left[\int_0^{\Delta t} B\sigma_z dt_1 + \int_{\Delta t}^{2\Delta t} -B\sigma_z dt_1\right] \\ &= \frac{1}{2\Delta t}\left[B\sigma_z \Delta t - B\sigma_z \Delta t\right] \\ &= 0. \end{aligned} \tag{2.3}$$

The higher order contributions to the average Hamiltonian all depend on the commutator $[\widetilde{H}_0(t'), \widetilde{H}_0(t)]$. Since $\widetilde{H}_0$ is at every time either $B\sigma_z$ or $-B\sigma_z$, this commutator is always zero, which means that $\bar{H}_0$ is exactly zero, so $\widetilde{U}(2\Delta t) = \mathbb{I}$, as desired.

In order to better understand the effect of the control sequences, beyond the insight offered by the terms in $\bar{H}_0$, we have used MATLAB to evaluate the propagator explicitly. As our measure of success in achieving the desired control result $U(T_c) = \mathbb{I}$ we use the gate entanglement fidelity F_e [61]-[63]. For unitary operations this can be expressed in terms of the physical-frame propagator in

the following way [64]:

$$F_e(t) = \left| tr\left\{ \frac{U(t)}{d} \right\} \right|^2 \tag{2.4}$$

where d is the dimension of the system; here $d = 2$. F_e is linearly related to the average of the input-output fidelity $F_{|\psi\rangle}(t) = |\langle\psi|U(t)|\psi\rangle|^2$ over all $|\psi\rangle$, which measures the overlap between an initial state and the final state after the propagator is applied. Perfect decoupling corresponds to $F_e = 1$. Dealing with the average as such gives F_e the advantage of being state-independent; we can perform a single, simple computation and not run the risk of selecting an initial state which has atypical behavior.

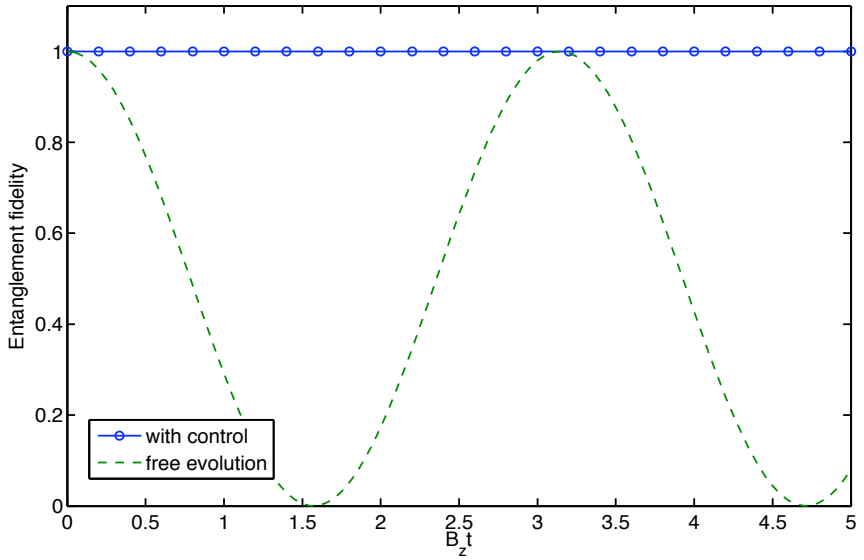

Figure 2.1: Entanglement fidelity vs. time for a qubit in a constant magnetic field in the z-direction, $B_z = 1$, with control scheme consisting of two X pulses, applied every $\Delta t = 0.1$. The markers on the plot indicate the times at which F_e was measured–i.e. every T_c.

The result of the control scheme described above, which succeeds at effecting $\bar{H}_0 = 0$ exactly, is shown in Figure 2.1. Each point on the control plot represents evalutation of F_e; it is important to note that the line connecting them is for visualization only, and does not represent the intermediate evolution. The effect is completely independent of either the magnitude of the magnetic field or the control timescale Δt, which is not generally the case in any more complicated situation. For a Δt which produces a cycle time T_c longer than the natural period T of the system, however, using dynamical decoupling ceases to be advantageous, since one in principle could simply sample the free system every T, when F_e has again returned to a value of unity. The oscillatory behavior also

means that, in the controlled system, one can have a confluence between the natural timescale and control timescale when $\Delta t = T$, since in this case the system has no net evolution during the "free" part of the cycle between pulses. This is not noticeable here because the averaging is perfect no matter what the value of Δt, but we will see the effects of this resonance in other situations. One should also note that the effectiveness of the control is independent of the placement of the pulses within the control cycle, so long as the qubit spends an equal amount of time with $\widetilde{H}_0 = B\sigma_z$ and $\widetilde{H}_0 = -B\sigma_z$. In more complicated settings this will be true to lowest order (in the $\bar{H}_0^{(0)}$ term), but here we still have $\bar{H}_0 = 0$ exactly. In particular, the following pulse sequence, in which the pulse takes place in the middle of the Δt interval, is also equivalent:

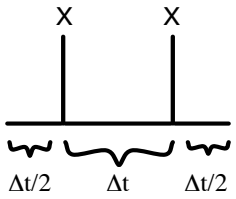

This sequence, known as the Carr-Purcell sequence [65], possesses time-reversal symmetry in the sense that $U_c(T_c - t) = U_c(t)$, which will play a special role in the following. Proof-of-principle demonstrations of the effectiveness of this sequence at suppressing single-photon decoherence have been given in [66] and [67].

2.2 First-order decoupling with finite amplitude: The simplest Eulerian cycle

The control scheme we have so far been considering involves instantaneous changes in the control propagator $U_c(t)$, which physically implies rotating the qubit instaneously through a finite angle. Effecting this change would require a control Hamiltonian with unbounded amplitude to be applied for zero time, which is not physically realizable. In reality, the control Hamiltonian required to perform such a rotation will have a finite amplitude, and will be applied for a finite time; furthermore, for the reasons given in the introduction, we may wish to make the amplitude of the control as small as possible. How effective is it to use the same XX sequence with pulses of finite amplitude? That is, consider a sequence in which each pulse occupies a finite time τ within the control interval Δt,

and each has a constant amplitude π/τ, so that the net effect is still a π_x rotation. The total cycle time remains $T_c = 2\Delta t$ as before. The sequence can be pictured in the following way:

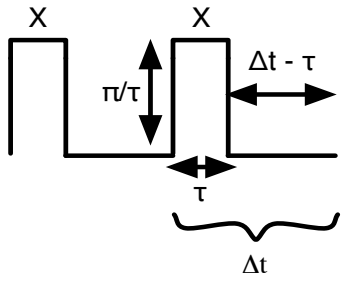

Thus, the control propagator for one cycle is as follows:

$$U_c(t) = \begin{cases} \mathbb{I} & 0 \le t < \Delta t - \tau \\ u_x(s) & \Delta t - \tau \le t < \Delta t \quad s \in [0, \tau] \\ \sigma_x & \Delta t \le t < 2\Delta t - \tau \\ u_x(s)\sigma_x & 2\Delta t - \tau \le t < 2\Delta t \quad s \in [0, \tau] \end{cases} \tag{2.5}$$

where $u_x(s) = \exp\{-i(\pi/\tau)(\sigma_x/2)s\}$. What is the average Hamiltonian now? As in the BB control scheme, we can see that $\bar{H}_0^{(0)} = 0$:

$$\begin{aligned} \bar{H}_0^{(0)} &= \frac{1}{2\Delta t}\int_0^{2\Delta t} U_c^\dagger(t_1) H_0 U_c(t_1) dt_1 \\ &= \frac{B}{2\Delta t}\left[\int_0^{\Delta t-\tau} \mathbb{I}\sigma_z\mathbb{I}\, dt_1 + \int_0^{\tau} u_x(t_1)^\dagger \sigma_z u_x(t_1) dt_1 + \int_{\Delta t}^{2\Delta t-\tau} \sigma_x\sigma_z\sigma_x dt_1 + \int_0^{\tau} \sigma_x u_x(t_1)^\dagger \sigma_z u_x(t_1)\sigma_x dt_1\right] \\ &= \frac{B}{2\Delta t}\left[\int_0^{\Delta t-\tau} \sigma_z\, dt_1 + \int_0^{\tau} u_x(t_1)^\dagger \sigma_z u_x(t_1) dt_1 - \int_{\Delta t}^{2\Delta t-\tau} \sigma_z dt_1 + \int_0^{\tau} u_x(t_1)^\dagger \sigma_x\sigma_z\sigma_x u_x(t_1) dt_1\right] \\ &= \frac{B}{2\Delta t}\left[\sigma_z(\Delta t - \tau) - \sigma_z(\Delta t - \tau) + \int_0^{\tau}\{u_x(t_1)^\dagger\sigma_z u_x(t_1) - u_x(t_1)^\dagger\sigma_z u_x(t_1)\} dt_1\right] \\ &= 0. \end{aligned}$$

That this cancellation still occurs, as reported in [32], can be understood by noting that the sequence $\{\sigma_x, \sigma_x\}$ is in fact an Eulerian cycle on the Cayley graph of our decoupling group $\mathcal{G} = \{\mathbb{I}, \sigma_x\}$. It will not be true in general that the naive transcription of a BB sequence is an Eulerian cycle, and we will see in the next chapter how poorly one BB sequence performs when we try to apply it with finite pulses. Here the coincidence is a result of the simplicity of the group and its graph: the number of

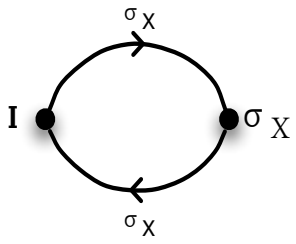

elements in the group, which determine the BB sequence, is the same as the number of edges, which determine the Euler sequence.

Going back to the $\bar{H}_0^{(0)}$ calculation above, we see there are effectively two kinds of cancellation at work: the direct cancellation we have seen previously, which results from the time-independent logical frame Hamiltonian acquiring a minus sign in the second part of the cycle, and a second type of cancellation, local in time, between the time-dependent logical frame Hamiltonians within the two pulses. The first is characteristic of BB decoupling, while the second is characteristic of Eulerian decoupling.

Unlike the BB scheme, $\bar{H}_0^{(1)}$ is no longer zero; the logical frame Hamiltonian does not commute with itself within a pulse. In this pulse sequence we lose $\bar{H}_0^{(1)}$ and all higher orders when the pulses become finite. For the first order term we find

$$\bar{H_0}^{(1)} = \frac{B_z^2 \sigma_x}{\pi} \tau \left(2 - \frac{\tau}{\Delta}\right). \tag{2.6}$$

As τ increases to occupy the full Δt, this term reaches its maximum value, and we therefore expect to find that the efficacy of the control scheme decreases, whereas in the limit where τ approaches zero we recover the perfect bang-bang result. The effect of increasing τ on F_e vs. time, for a fixed Δt, is shown in Figure 2.2. Indeed, we can see that F_e drops increasingly quickly as τ increases.

In order to better visualize this dependence, it is helpful to introduce as a measure the time it takes for the entanglement fidelity to drop below a certain threshold value. If the value is $F_e = 0.999$, for example, this time will be denoted $T_{.999}$. Because F_e can only be acquired stroboscopically, at the end of each cycle, and the cycle time is determined by Δt, this is not always a fair measure–F_e cannot be measured at exactly the same times for sequences with different Δt; nevertheless the nature of the dependence is clear. Figure 2.3 shows how $T_{.999}$ depends on τ for three different Δt values, including the one of Figure 2.2. The plot looks bumpy at large Δt for the reason given above:

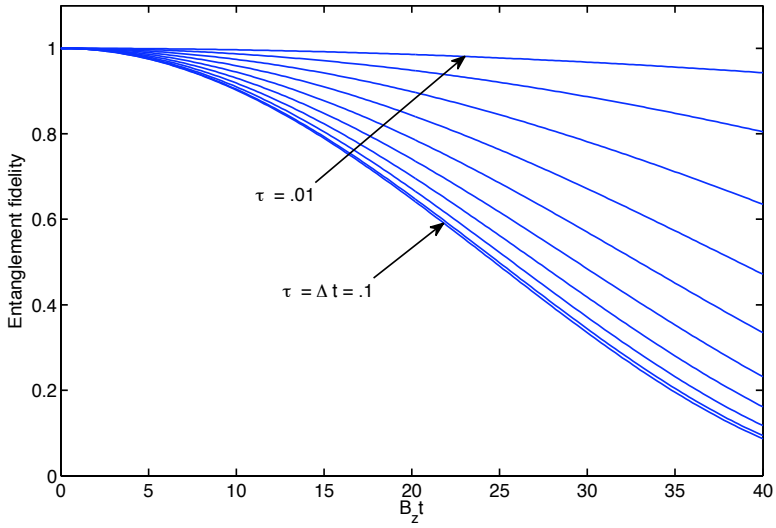

Figure 2.2: F_e vs. time for $\tau = 0.01, 0.02, ..., 0.1$ (from top to bottom), with fixed $\Delta t = 0.1$

as Δt changes, the times at which F_e can be measured also change, and in all cases these times can be no more finely grained than T_c.

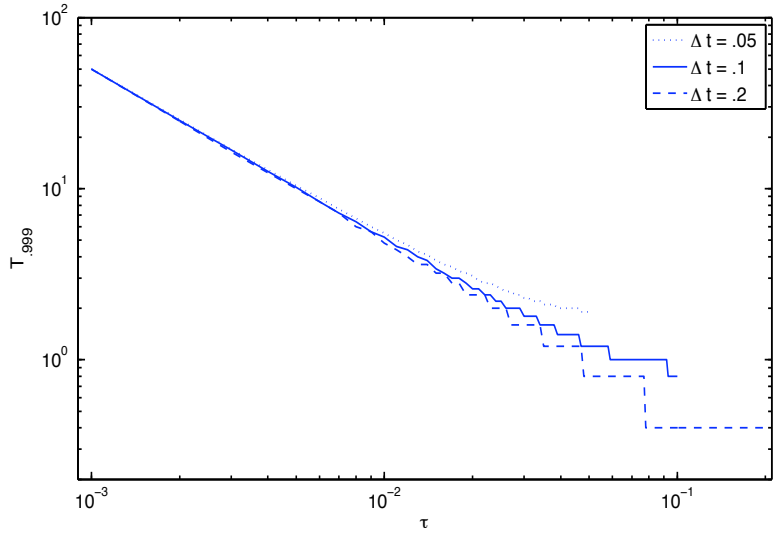

Figure 2.3: $T_{.999}$ vs. τ, with $\Delta t = 0.05, 0.1, 0.2$

We can see here that the relationship between $T_{.999}$ and τ is well-described by $T_{.999} \propto \tau^{-1}$. For $\tau \to 0$, $T_{.999} \to \infty$ for this system, clearly illustrating the impact of finite-width effects. We also see that varying Δt makes very little difference except for the region where $\tau \approx \Delta t$. Figure 2.4(a) shows the Δt dependence more explicitly; indeed we see that for $\Delta t \approx \tau$, increasing Δt causes a decay in

$T_{.75}$, but it quickly approaches an asymptotic value determined by τ. This can be understood by looking at $\bar{H}_0^{(1)}$ in (2.6); the factor $\tau(2 - \frac{\tau}{\Delta t})$ approaches the value 2τ as $\Delta t \to \infty$. If instead of

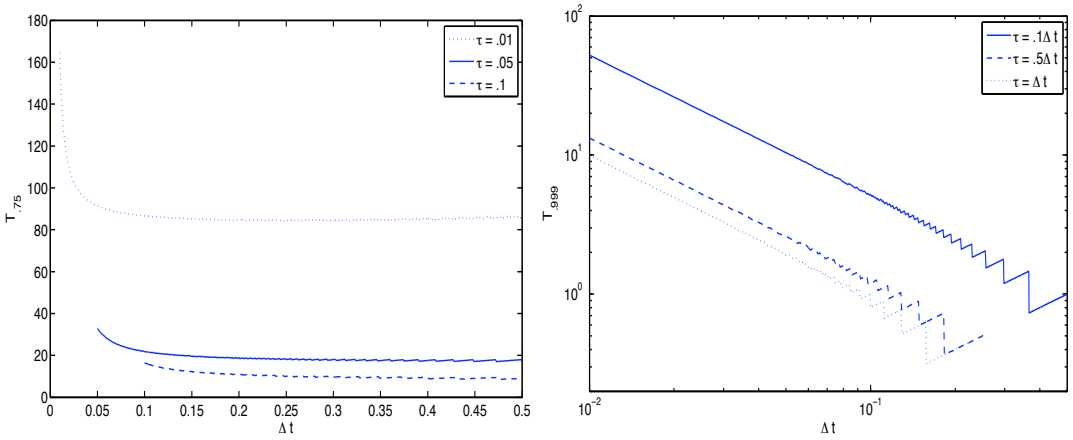

(a) Varying τ, with fixed $\Delta t = 0.1$

(b) $T_{.999}$ vs. τ for different Δt.

Figure 2.4: Qubit evolving in constant magnetic field $B_z = 1$, with control consisting of XX sequence with finite pulses.

varying Δt with a fixed τ we choose a τ which occupies a fixed fraction of Δt, as in Figure 2.4(b), we see that $T_{.999} \propto \Delta t^{-1}$, which we know is a result of the underlying τ dependence. When $\tau/\Delta t$ is smaller, the absolute value of $T_{.999}$ is higher, as expected, since in this case we approach the BB limit.

Plotting the entire $(\Delta t, \tau)$ space with $T_{.999}$ on the z-axis is a helpful way to visualize the overall dependence on Δt and τ; two views are shown in Figure 2.5.

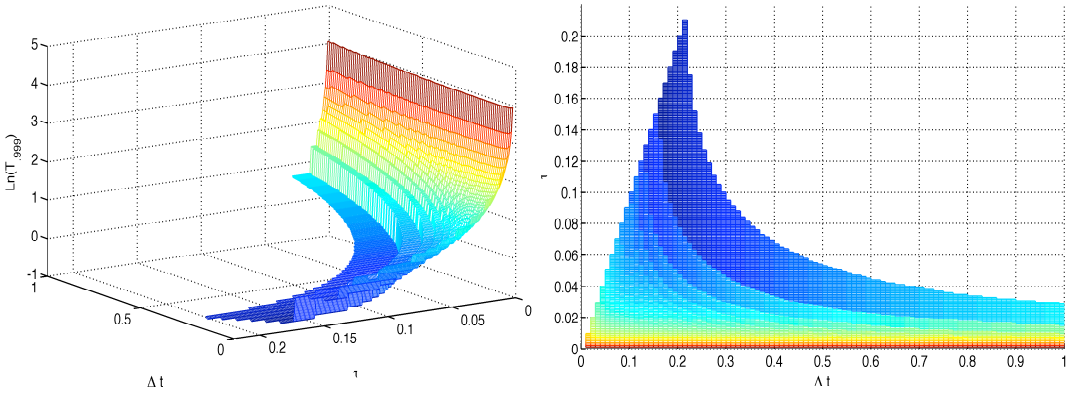

(a) Side view

(b) Overhead view

Figure 2.5: $T_{.999}$ vs. Δt and τ, for a qubit evolving in constant magnetic field $B_z = 1$. For each value of Δt, τ is in $(0, \Delta t]$

2.3 Second-order decoupling with finite amplitude: The simplest Eulerian supercycle

If we are fine with just $\bar{H}_0^{(0)} = 0$, as above, then as in the BB case we are free to choose the placement of the pulses within the control cycle; so long as the pulses are of equal duration and equal time is spent in $\widetilde{H}_0 = B\sigma_z$ and $\widetilde{H}_0 = -B\sigma_z$. However, a pulse sequence which is time-symmetric about the "center" of the cycle—that is, for which $U_c(t) = U_c(T_c - t)$—will cancel $\bar{H}_0^{(1)}$ and all other odd-ordered terms in the average Hamiltonian. An example of this can be seen by considering the Carr-Purcell sequence, in which the pulses are centered within each Δt interval. When finite pulses are considered, we may either keep the phases of the pulse propagators the same, as in the XX sequence above:

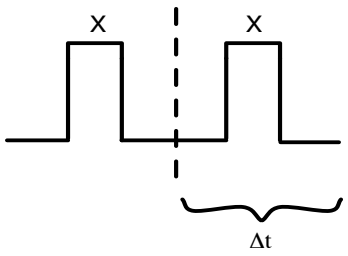

that is,

$$U_c(t) = \begin{cases} \mathbb{I} & 0 \le t < \Delta t/2 - \tau/2 \\ \exp\{-i(\pi/\tau)(\sigma_x/2)s\} & \Delta t/2 - \tau/2 \le t < \Delta t/2 + \tau/2 \quad s \in [0,\tau] \\ \sigma_x & \Delta t/2 + \tau/2 \le t < 3\Delta t/2 + \tau/2 \\ \exp\{-i(\pi/\tau)(\sigma_x/2)s\}\sigma_x & 3\Delta t/2 + \tau/2 \le t < 3\Delta t/2 + 3\tau/2 \quad s \in [0,\tau] \\ \mathbb{I} & 3\Delta t/2 + 3\tau/2 \le t < 2\Delta t \end{cases} \tag{2.7}$$

or we can allow one pulse to have opposite phase:

$$U_c(t) = \begin{cases} \mathbb{I} & 0 \le t < \Delta t/2 - \tau/2 \\ \exp\{-i(\pi/\tau)(\sigma_x/2)s\} & \Delta t/2 - \tau/2 \le t < \Delta t/2 + \tau/2 \quad s \in [0,\tau] \\ \sigma_x & \Delta t/2 + \tau/2 \le t < 3\Delta t/2 + \tau/2 \\ \exp\{+i(\pi/\tau)(\sigma_x/2)s\}\sigma_x & 3\Delta t/2 + \tau/2 \le t < 3\Delta t/2 + 3\tau/2 \quad s \in [0,\tau] \\ \mathbb{I} & 3\Delta t/2 + 3\tau/2 \le t < 2\Delta t \end{cases} \tag{2.8}$$

The former sequence, as we have seen, has $\bar{H}_0^{(0)} = 0$, but $\bar{H}_0^{(1)} \neq 0$, given in Eq. (2.6). The latter sequence, on the other hand, has $\bar{H}_0^{(1)} = 0$, but now

$$\bar{H}_0^{(0)} = \frac{2B_z}{\pi}\left(\frac{\tau}{\Delta t}\right)\sigma_y. \tag{2.9}$$

It turns out that by combining the two types of symmetry into a four-pulse "supercycle", we can cancel both $\bar{H}_0^{(0)}$ and $\bar{H}_0^{(1)}$:

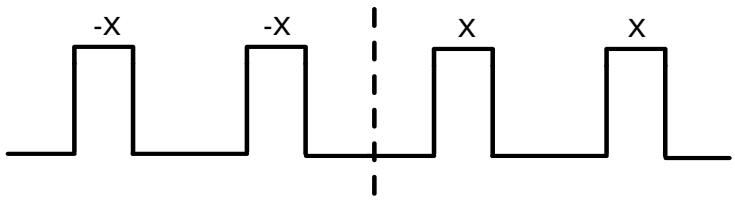

That is,

$$U_c(t) = \begin{cases} \mathbb{I} & 0 \le t < \Delta t - \tau \\ \exp\{-i(\pi/\tau)(\sigma_x/2)s\} & \Delta t - \tau \le t < \Delta t \quad s \in [0,\tau] \\ \sigma_x & \Delta t \le t < 2\Delta t - \tau \\ \exp\{-i(\pi/\tau)(\sigma_x/2)s\}\sigma_x & 2\Delta t - \tau \le t < 2\Delta t \quad s \in [0,\tau] \\ \mathbb{I} & 2\Delta t \le t < 3\Delta t - \tau \\ \exp\{+i(\pi/\tau)(\sigma_x/2)s\} & 3\Delta t - \tau \le t < 3\Delta t \quad s \in [0,\tau] \\ \sigma_x & \Delta t \le t < 4\Delta t - \tau \\ \exp\{+i(\pi/\tau)(\sigma_x/2)s\}\sigma_x & 4\Delta t - \tau \le t < 4\Delta t \quad s \in [0,\tau] \end{cases} \tag{2.10}$$

The two same-phase "++" and "−−" pieces individually cancel $\bar{H}_0^{(0)}$, so $\bar{H}_0^{(0)} = 0$ for the cycle; in addition, the sequence is also time-symmetric about the midpoint, so we find that $\bar{H}_0^{(1)} = 0$. This is known in NMR spectroscopy research, and is the sequence which Haeberlen [11] refers to as "alternating pairs of pulses." For us it represents the simplest example of an Euler supercycle. Figure 2.6(a) shows the effect of increasing τ with this sequence, analogous to Figures 2.2 for the two-pulse sequence. Although the two plots look similar, note the difference in scale. The inset shows a comparison between the two sequences with $\Delta t = \tau = .1$; in the time it takes for F_e to go to zero with the two-pulse sequence, the drop in F_e with the supercycle is almost imperceptible.

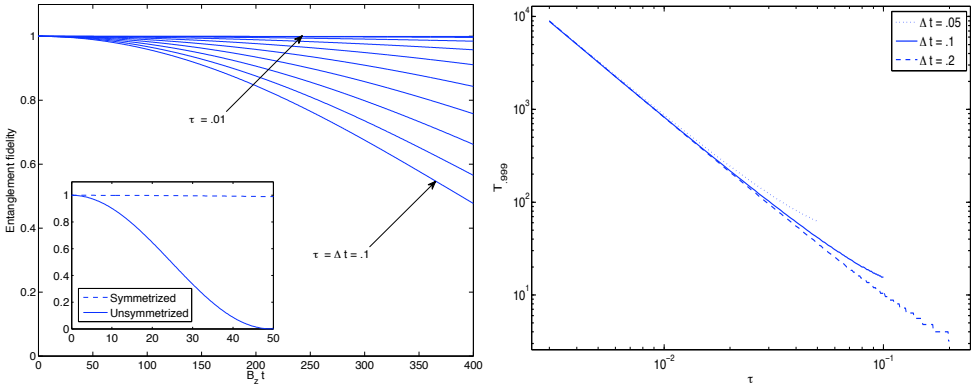

(a) Fixed $\Delta t = .1$, for various values of τ.

(b) $T_{.999}$ vs. τ for different Δt.

Figure 2.6: Qubit evolving in constant magnetic field $B_z = 1$, with control consisting of symmetrized Carr-Purcell.

Figure 2.6(b) shows $T_{.999}$ vs. τ for a few values of Δt, analogous to Figure 2.3. In this case we see that $T_{.999} \propto \tau^{-2}$. That is, $T_{.999}$ actually decays more quickly with τ than the two-pulse sequence, but we should keep in mind that the absolute value of $T_{.999}$ is always greater in this case. As before, we see that changing Δt has very little effect except where $\tau \approx \Delta t$. Indeed, Figure 2.7 shows $T_{.75}$ vs. Δt for a few different values of τ, and we see behavior very similar to the two-pulse case in Figure 2.4(a). This behavior was understood previously by looking at $\bar{H}_0^{(1)}$; it is especially interesting here because $\bar{H}_0^{(0)}$ and $\bar{H}_0^{(1)}$ are both zero in this case, and we do not have an analytical expression for $\bar{H}_0^{(2)}$, so we only have "experimental" access to it. That the dependence on τ and Δt for the two sequences is so similar suggests that $\bar{H}_0^{(2)}$ for the supercycle has a form similar to $\bar{H}_0^{(1)}$ for the two-pulse sequence, in Eq. (2.6), perhaps with an extra power of τ to account for the $T_{.999} \propto \tau^{-2}$ relationship.

Figure 2.8 shows the $(\Delta t, \tau)$ space for the supercycle—note that this time we use $T_{.9999}$—again

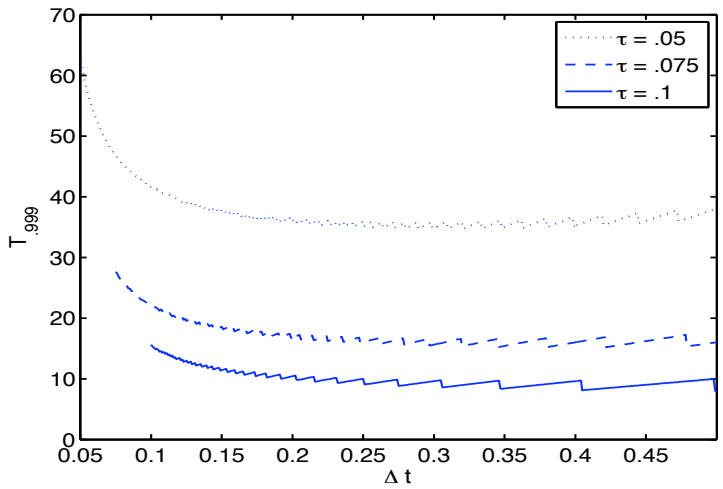

Figure 2.7: Time for entanglement fidelity to drop below a threshold value of .9999 for qubit evolving in constant magnetic field $B_z = 1$, with control consisting of symmetrized Carr-Purcell.

supporting the assessment that the supercycle shares a similar τ and Δt structure with the two pulse sequence, simply with a greater absolute value for F_e at all times.

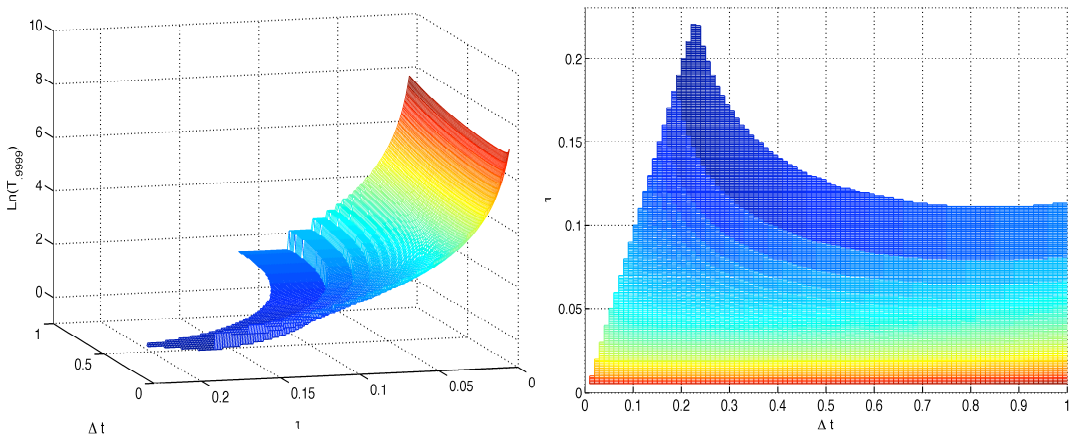

(a) Side view

(b) Overhead view

Figure 2.8: $T_{.9999}$ vs. Δt and τ, for a qubit evolving in constant magnetic field $B_z = 1$. For each value of Δt, τ is in $(0, \Delta t]$

An explicit comparison between the symmetrized and unsymmetrized sequences—that is, between cancelling both $\bar{H}_0^{(0)}$ and $\bar{H}_0^{(1)}$, or just $\bar{H}_0^{(0)}$, respectively—is shown in Figures 2.9(a) and 2.9(b).

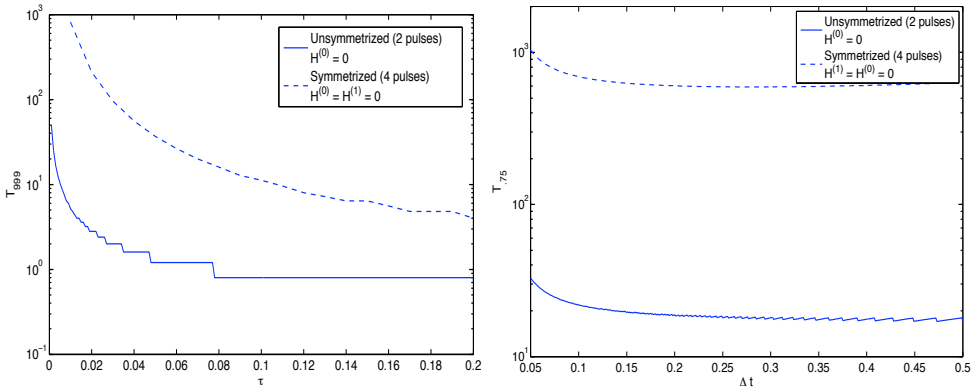

(a) $T_9 99$ vs. τ with fixed $\Delta t = 0.1$.

(b) $T_7 5$ vs. Δt with $\tau = 0.05$

Figure 2.9: Comparison between symmetrized and unsymmetrized Carr-Purcell sequences.

Thus, we have seen the effect that increasing the width of the pulses may have, and that cancellation of higher orders in the average Hamiltonian through time-reversal symmetry does indeed lead to superior performance. In the next chapter we will explore the same considerations in a more general setting.

Chapter 3

Control of Unknown Single-Qubit Dynamics

Because the exact direction of the magnetic field may be unknown, and simply for greater generality, we now consider the more complicated case in which the qubit's natural Hamiltonian has components in all directions:

$$H_0 = \vec{B} \cdot \vec{\sigma} = B_x\sigma_x + B_y\sigma_y + B_z\sigma_z.$$

The propagator corresponding to this Hamiltonian is given by

$$U(t) = \exp\{-i(\vec{B} \cdot \vec{\sigma})t\} = \cos(|B|t)\mathbb{I} - i\sin(|B|t)\hat{n} \cdot \vec{\sigma} \tag{3.1}$$

where $\hat{n} = \vec{B}/|B|$. As in the previous case, we can see that this propagator has a natural period of $T = 2\pi/|B|$, and returns to the identity up to a phase factor after $T = \pi/|B|$, meaning that the entanglement fidelity computed from it will have a period $T = \pi/|B|$. An example of this will be shown in Figure 3.1(a).

3.1 First-order bang-bang decoupling

In the bang-bang limit, in order to cancel $\bar{H}_0^{(0)}$, the control must move through the entire Pauli group $\{\mathbb{I}, \sigma_x, \sigma_y, \sigma_z\}$, so a minimum of four pulses are required and the cycle time is increased to

$4\Delta t$. Different pulse sequences are possible, depending on the path one chooses for traversing $\mathcal{G}$. For example, we will here choose the path $\{\mathbb{I}, \sigma_x, \sigma_z, \sigma_y\}$; that is,

$$U_c(t) = \begin{cases} \mathbb{I} & 0 \leq t < \Delta t \\ \sigma_x & \Delta t \leq t < 2\Delta t \\ \sigma_z & 2\Delta t \leq t < 3\Delta t \\ \sigma_y & 3\Delta t \leq t < 4\Delta t. \end{cases} \tag{3.2}$$

Since the pulse required to transition from element g_l to g_{l+1} is given by $g_{l+1}g_l^\dagger$, this corresponds to the pulse sequence $\{\sigma_x, \sigma_y, \sigma_x, \sigma_y\}$, which we will denote XYXY. That is, the propagator for one cycle in the physical frame is given by

$$U(4\Delta t) = P_4 e^{-iH_0\Delta t} P_3 e^{-iH_0\Delta t} P_2 e^{-iH_0\Delta t} P_1 e^{-iH_0\Delta t} \tag{3.3}$$

where $P_1 = P_3 = e^{-i\pi\sigma_x/2}$ and $P_2 = P_4 = e^{-i\pi\sigma_y/2}$, which can be pictured in the following way, recalling again that the forward time direction is to the left:

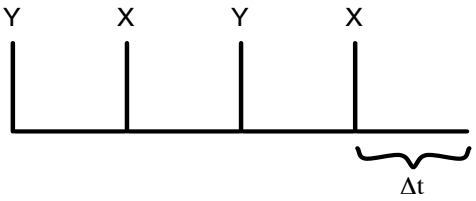

What is the average Hamiltonian in this case? The zeroth order contribution is

$$\begin{aligned} \bar{H}_0^{(0)} &= \frac{1}{4\Delta t}\int_0^{4\Delta t} U_c^\dagger(t_1) H_0 U_c(t_1) dt_1 \\ &= \frac{1}{4\Delta t}\left[\int_0^{\Delta t} \mathbb{I} H_0 \mathbb{I}\, dt_1 + \int_{\Delta t}^{2\Delta t} P_1^\dagger H_0 P_1 dt_1 + \int_{2\Delta t}^{3\Delta t} (P_2P_1)^\dagger H_0 P_2P_1 dt_1 + \int_{3\Delta t}^{4\Delta t} (P_3P_2P_1)^\dagger H_0 P_3P_2P_1 dt_1\right] \\ &= \frac{1}{4\Delta t}[(B_x\sigma_x + B_y\sigma_y + B_z\sigma_z)\Delta t + (B_x\sigma_x - B_y\sigma_y - B_z\sigma_z)\Delta t \\ &\quad +(-B_x\sigma_x - B_y\sigma_y + B_z\sigma_z)\Delta t + (-B_x\sigma_x + B_y\sigma_y - B_z\sigma_z)\Delta t] \\ &= 0 \end{aligned} \tag{3.4}$$

as expected, since the BB prescription is designed to do this. For the first order contribution, the

form of which is given in Eq. (1.9), we find

$$\bar{H}_0^{(1)} = B_x B_y \sigma_z \Delta t. \tag{3.5}$$

Note the explicit dependence on Δt—higher order terms will be dependent on higher powers of Δt. As $\Delta t \to 0$, $\bar{H}^{(j)} \to 0, j \geq 1$, so the efficacy of the control scheme is increased as the pulses are applied more frequently. Figure 3.1(a) shows the entanglement fidelity vs. time with this control sequence for different values of Δt, as well as the free evolution. The tick marks on the plots indicate the end of each cycle, where F_e can be measured—we emphasize again that the line connecting them is for visualization purposes only, and does not represent the intermediate evolution of F_e.

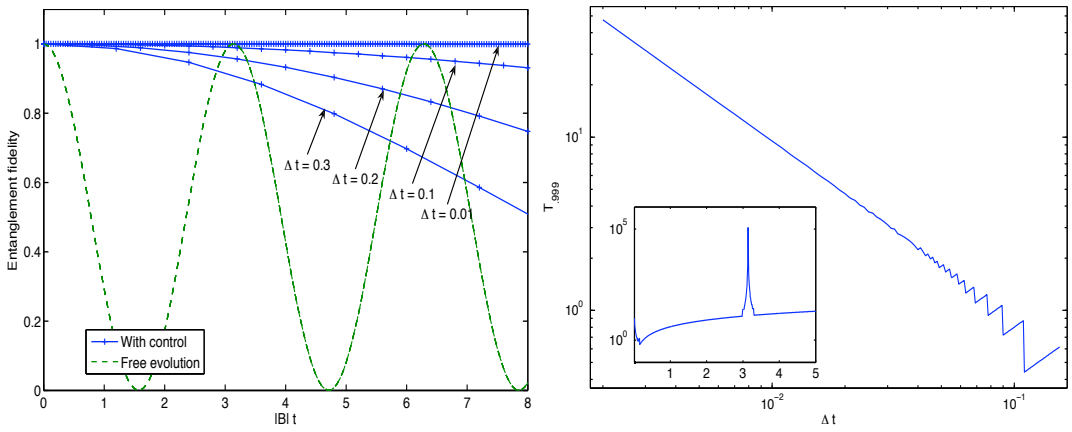

(a) F_e vs. time for different Δt

(b) $T_{.999}$ vs. Δt

Figure 3.1: BB sequence XYXY

Figure 3.1(b) shows how $T_{.999}$, the time for F_e to drop below .999, depends on Δt. We see here the relationship $T_{.999} \propto \Delta t^{-1}$, recalling the nature of the τ dependence in the case of the finite-amplitdue XX sequence in the previous chapter. This is strongly suggestive that if the first nonzero term in $\bar{H}_0$ depends linearly on Δt or τ, then $T_{.999}$ will vary with Δt^{-1} or τ^{-1}, respectively. The inset shows $T_{.999}$ for larger values of Δt, to illustrate what happens when the control timescale Δt and natural timescale T coincide. At $\Delta t = \pi$, we see a peak in $T_{.999}$ which is several orders of magnitude higher than the surrounding values; that is, for which the results are nearly perfect. This can be understood by recalling the periodicity in the free evolution. The sequence consists of four periods of free evolution of duration Δt punctuated by the pulses; when $\Delta t = \pi$, then in each of the Δt intervals there is no net evolution.

3.2 First-order bounded-strength decoupling

3.2.1 Naive bounded control

As already remarked, the instantaneous pulses we have used to achieve this cancellation are not physically realizable. What happens if try to naively transcribe the BB sequence described above–XYXY–for use with bounded-strength control, in which the pulses each have finite amplitude and finite duraction τ? That is, consider a sequence which looks like:

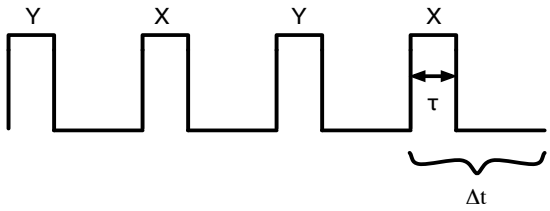

with control propagator:

$$U_c(t) = \begin{cases} \mathbb{I} & 0 \leq & t & < \Delta t - \tau & \\ \exp\{-i(\pi/\tau)(\sigma_x/2)s\} \cdot \mathbb{I} & \Delta t - \tau \leq & t & < \Delta t & s \in [0,\tau] \\ \sigma_x & \Delta t \leq & t & < 2\Delta t - \tau & \\ \exp\{-i(\pi/\tau)(\sigma_y/2)s\} \cdot \sigma_x & 2\Delta t - \tau \leq & t & < 2\Delta t & s \in [0,\tau] \\ \sigma_z & 2\Delta t \leq & t & < 3\Delta t - \tau & \\ \exp\{-i(\pi/\tau)(\sigma_x/2)s\} \cdot \sigma_z & 3\Delta t - \tau \leq & t & < 3\Delta t & s \in [0,\tau] \\ \sigma_y & 3\Delta t \leq & t & < 4\Delta t - \tau & \\ \exp\{-i(\pi/\tau)(\sigma_y/2)s\} \cdot \sigma_y & 4\Delta t - \tau \leq & t & < 4\Delta t & s \in [0,\tau] \end{cases} \tag{3.6}$$

Computing the average Hamiltonian, we see that this time we lose even $\bar{H}_0^{(0)}$, which becomes

$$\bar{H}_0^{(0)} = -\left(\frac{B_x + B_y}{\pi}\right)\left(\frac{\tau}{\Delta t}\right)\sigma_z. \tag{3.7}$$

The effect of taking this naive XYXY sequence and increasing the value of τ for a fixed value of Δt is shown in Figure 3.2(a), with very small values of τ, and Figure 3.2(b), with slightly larger values of τ. This is divided into two different figures because, interestingly, for very small values of τ the performance is actually improved over the bang-bang ($\tau = 0$) case, up to a critical value

τ_{max}. Figure 3.2(a) shows these values of τ; note that the worst performance in this figure actually occurs for the smallest value of τ. In Figure 3.2(b) we see values of τ which are greater than τ_{max}, so that the performance now decreases with increasing τ. This non-monotonic dependence on τ is also captured in Figure 3.2(c), which shows the value of the entanglement fidelity at a fixed time vs. τ and, in the inset, T_{999} vs. τ.

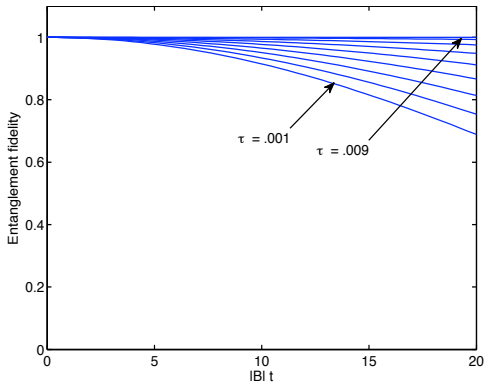

(a) F_e vs. time with $\Delta t = .1$, for values of τ between .001 and τ_{max}, which in this case is close to .009. The plot which goes to zero most quickly actually has the smallest value of τ; looking at the plots from bottom to top represents increasing values of τ.

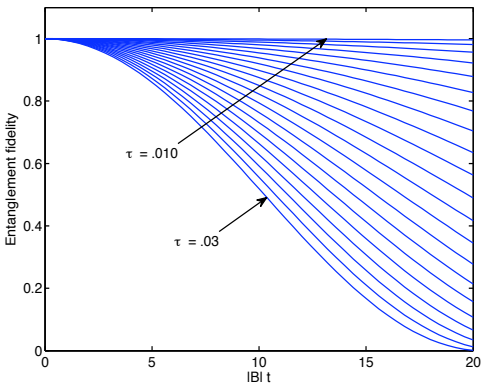

(b) F_e vs. time with $\Delta t = .1$, for values of τ larger than τ_{max}. Now the smallest value of τ is at the top, and increasing τ moves in the downward direction.

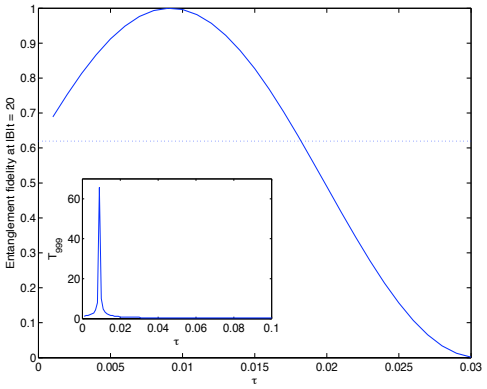

(c) F_e at a fixed time vs. tau with$\Delta t = 0.1$; like taking a "slice" down the right hand side of Figures 3.2(a) and 3.2(b), the time at which F_e is measured is the final time shown in these figures. The dotted line indicates the value of F_e at this time if bang-bang ($\tau = 0$) control were used. Thus, for a certain range of τ values, control with finite pulses is actually better than bang-bang control. The inset shows T_{999} vs. τ, with $\Delta t = .1$.

Figure 3.2: Performance of naive XYXY sequence with finite pulses

The story can be visually summarized by looking at the entire $(\Delta t, \tau)$ parameter space; that is, the time for the entanglement fidelity to drop below a threshold value vs. Δt and τ. This is shown in Figure 3.3, where we see a "ridge" of high-performing values of Δt and τ. The shape can be understood by considering the competition between $\bar{H}_0^{(0)}$, see Eq. (3.7), and $\bar{H}_0^{(1)}$, in which the dominant contribution is given by $\bar{H}_0^{(1)}$ for the BB sequence, see Eq. (3.5). That the $\bar{H}_0^{(0)}$ term is negative means that there are values for Δt and τ for which $\bar{H}_0^{(0)}$ and $\bar{H}_0^{(1)}$ happen to cancel each other. Setting the magnitudes of these terms equal yields a value for τ_{max} in terms of Δt and $\vec{B}$ which agrees very well with the observed value,

$$\tau_{max} \approx \frac{\pi B_x B_y}{B_x + B_y} \Delta t^2. \tag{3.8}$$

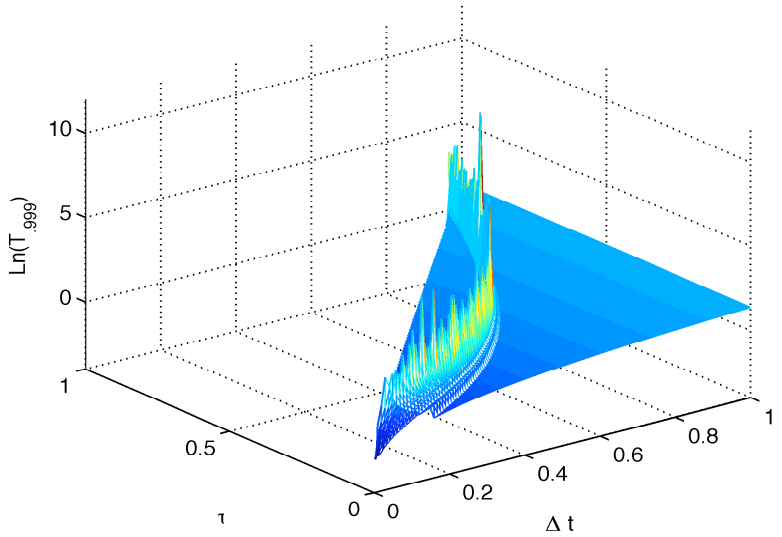

Figure 3.3: Time for F_e to drop below .999 vs. Δt and τ, showing the true extent of the nonmonotonic dependence on τ. The "ridge" represents non-zero values of τ for each Δt which exceed the peformance of even the bang-bang case.

Figure 3.4 is offered as further illustration of this rather surprising behavior, showing the entanglement fidelity vs. time with a relatively large value of Δt for three different values of τ: one which is on the ridge, and two which are not. One would expect in general that increasing τ and Δt would monotonically decrease performance, but here the striking improvement in performance which results when $\bar{H}_0^{(0)}$ and $\bar{H}_0^{(1)}$ cancel each other is evident, as with the "right" value ot τ the entanglement fidelity remains indistinguishable from unity at a value of Δt which is quite large. It should be noted that the cancellation between $\bar{H}_0^{(0)}$ and $\bar{H}_0^{(1)}$ is likely an artifact of the simple

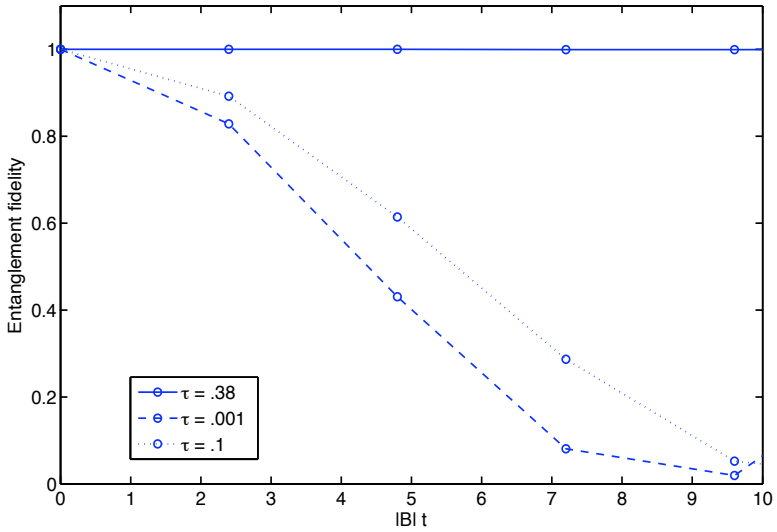

Figure 3.4: Entanglement fidelity vs. time with $\Delta t = 0.6$, for values of τ both on ($\tau = 0.38$ and off ($\tau = 0.001, 0.01$) the "ridge" of high performance.

system we are considering, and the nonmonotonic behavior probably would not be observed in a more general open-system setting, but it would be interesting to see if this suspicion is confirmed.

3.2.2 Eulerian control

With the naive transcription of the BB XYXY sequence with finite pulses considered above, we saw that $\bar{H}_0^{(0)} \neq 0$–what happened? Notice that the XYXY sequence, which corresponds to the path $\{\sigma_x, \sigma_y, \sigma_x, \sigma_y\}$, does not represent an Eulerian cycle on the Cayley graph of the decoupling group $\mathcal{G} = \{\mathbb{I}, \sigma_x, \sigma_y, \sigma_z\}$, where in this context the path is taken to be a set of edges. The graph is shown here for our choice of generating set $\Gamma = \{\sigma_x, \sigma_y\}$:

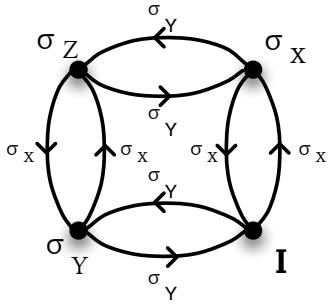

Each vertex has two outgoing edges, one corresponding to each generator, so a full Eulerian cycle involves traversing each of the eight edges exactly once. For example, $\mathcal{E}_1 = \{\sigma_x, \sigma_y, \sigma_x, \sigma_y, \sigma_y, \sigma_x, \sigma_y, \sigma_x\}$ and $\mathcal{E}_2 = \{\sigma_x, \sigma_y, \sigma_y, \sigma_x, \sigma_y, \sigma_x, \sigma_x, \sigma_y\}$ are among the Eulerian cycles on this graph, where it is understood that each path begins at the identity. That is, an appropriate control sequence for canceling $\bar{H}_0^{(0)}$ with finite pulses may consist of XYXYYXYX. The intuition we have is that, with bang-bang control, canceling $\bar{H}_0^{(0)}$ may be achieved by realizing just the vertices of the graph of the decoupling group—that is, "jumping" from one group element to another—whereas with finite amplitude control we must actually traverse the edges of the graph, where the number of edges is proportional to both the number of elements in the group and the number of elements in a generating set. The manner in which this approach cancels $\bar{H}_0^{(0)}$ can be seen here for the control sequence XYXYYXYX, where we have chosen to implement each generator by a control Hamiltonian which is piecewise constant and corresponds to a square pulse of duration τ at the end of each Δt interval, similar to the other finite pulses we have so far been considering:

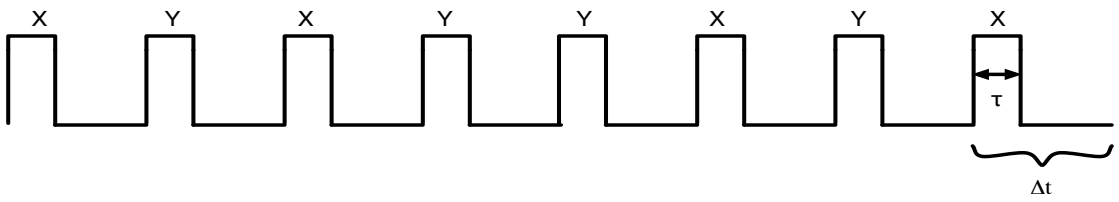

corresponding to the control propagator:

$$
U_c(t) = \begin{cases}
\mathbb{I} & 0 \leq & t & < \Delta t - \tau & \\
\exp\{-i(\pi/\tau)(\sigma_x/2)s\} \cdot \mathbb{I} & \Delta t - \tau \leq & t & < \Delta t & s \in [0, \tau] \\
\sigma_x & \Delta t \leq & t & < 2\Delta t - \tau & \\
\exp\{-i(\pi/\tau)(\sigma_y/2)s\} \cdot \sigma_x & 2\Delta t - \tau \leq & t & < 2\Delta t & s \in [0, \tau] \\
\sigma_z & 2\Delta t \leq & t & < 3\Delta t - \tau & \\
\exp\{-i(\pi/\tau)(\sigma_x/2)s\} \cdot \sigma_z & 3\Delta t - \tau \leq & t & < 3\Delta t & s \in [0, \tau] \\
\sigma_y & 3\Delta t \leq & t & < 4\Delta t - \tau & \\
\exp\{-i(\pi/\tau)(\sigma_y/2)s\} \cdot \sigma_y & 4\Delta t - \tau \leq & t & < 4\Delta t & s \in [0, \tau] \\
\mathbb{I} & 4\Delta t \leq & t & < 5\Delta t - \tau & \\
\exp\{-i(\pi/\tau)(\sigma_y/2)s\} \cdot \mathbb{I} & 5\Delta t - \tau \leq & t & < 5\Delta t & s \in [0, \tau] \\
\sigma_y & 5\Delta t \leq & t & < 6\Delta t - \tau & \\
\exp\{-i(\pi/\tau)(\sigma_x/2)s\} \cdot \sigma_y & 6\Delta t - \tau \leq & t & < 6\Delta t & s \in [0, \tau] \\
\sigma_z & 6\Delta t \leq & t & < 7\Delta t - \tau & \\
\exp\{-i(\pi/\tau)(\sigma_y/2)s\} \cdot \sigma_z & 7\Delta t - \tau \leq & t & < 7\Delta t & s \in [0, \tau] \\
\sigma_x & 7\Delta t \leq & t & < 8\Delta t - \tau & \\
\exp\{-i(\pi/\tau)(\sigma_x/2)s\} \cdot \sigma_x & 8\Delta t - \tau \leq & t & < 8\Delta t & s \in [0, \tau]
\end{cases} \tag{3.9}
$$

We can see that this gives $\bar{H}_0^{(0)} = 0$:

$$\begin{aligned}
\bar{H}_0^{(0)} &= \frac{1}{8\Delta t}\int_0^{8\Delta t} U_c^\dagger(t) H_0 U_c(t) dt \\
&= \frac{1}{8\Delta t}\Bigg\{ \int_0^{\Delta t-\tau} 2\left(\mathbb{I}\, H_0\, \mathbb{I} + \sigma_x H_0 \sigma_x + \sigma_y H_0 \sigma_y + \sigma_z H_0 \sigma_z\right) dt \\
&\qquad + \int_0^{\tau} (\mathbb{I}\, u_x^\dagger(t) H_0 u_x(t)\, \mathbb{I} + \sigma_x\, u_x^\dagger(t) H_0 u_x(t)\, \sigma_x + \sigma_y\, u_x^\dagger(t) H_0 u_x(t)\, \sigma_y + \sigma_z\, u_x^\dagger(t) H_0 u_x(t)\, \sigma_z \\
&\qquad\qquad + \mathbb{I}\, u_y^\dagger(t) H_0 u_y(t)\, \mathbb{I} + \sigma_x\, u_y^\dagger(t) H_0 u_y(t)\, \sigma_x + \sigma_y\, u_y^\dagger(t) H_0 u_y(t)\, \sigma_y + \sigma_z\, u_y^\dagger(t) H_0 u_y(t)\, \sigma_z)\, dt \Bigg\} \\
&= 0.
\end{aligned}$$

As in the case of the XX sequence with finite pulses, there are two types of cancellation at work: in the first integral we see the contributions from the intervals of free evolution between the pulses, which cancel each other in the non-local BB fashion, while in the second integral we see the contributions from the evolution within the pulses, which cancel each other locally in time. The terms within the second integral are divided into two "families," one corresponding to each generator, and each of which has four terms, corresponding to the four group elements. This structure is the reason why the Euler sequence succeeds where the naive XYXY sequence fails; averaging over the entire group for each of $u_x^\dagger(t) H_0 u_x(t)$ and $u_y^\dagger(t) H_0 u_y(t)$ is necessary for cancellation.

In the original proof of the Euler averaging [42], it was assumed that each generator would be realized by the same control Hamiltonian each time it occurred along the cycle, as above. However, there is nothing which requires this *a priori*; when we consider square pulses with duration $\tau < \Delta t$, for example, there is in principle some freedom regarding the placement of the pulse within the Δt. In fact, we can even consider the possibility of using a different control Hamiltonian each time a generator is implemented; for example, using different locations for the pulses used to realize X rotations in the same cycle. What are the restrictions on this freedom? So long as the pulses are of the same duration and the sequence corresponds to an Euler cycle, the contribution to $\bar{H}_0^{(0)}$ from the evolution within the pulses will be zero. For the intervals of free evolution, the requirement is that the system spends equal time in each of the four different logical frame Hamiltonians. So, in addition to the–perhaps most obvious–placement of pulses in the $\bar{H}_0^{(0)}$ calculation above, the following sequence also gives $\bar{H}_0^{(0)} = 0$:

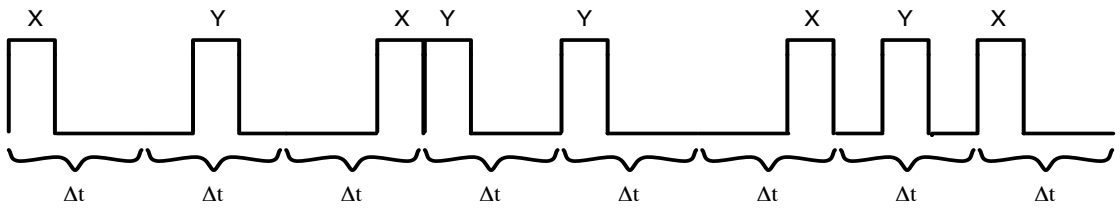

This sequence is known affectionately as the "perverse" Euler, so-called because effective pulse sequences are typically based on symmetry; the apparently random placement of the pulses seems to violate our symmetry sensibilities. Since both sequences have the Eulerian structure, however, from the perspective of $\bar{H}_0^{(0)}$ they are equally good. How does the placement of the pulses affect $\bar{H}_0^{(1)}$? For the usual Euler, we find

$$\bar{H}_0^{(1)} = -\tau \frac{B_y(B_x + B_y)}{\pi}\sigma_x - \tau \frac{B_x(B_x + B_y)}{\pi}\sigma_y \tag{3.10}$$

while for the "perverse" Euler we find

$$\bar{H}_0^{(1)} = -\left[\tau \frac{B_y(B_x + B_y)}{\pi} - \frac{3}{4}B_y B_z(\Delta t - \tau)\right]\sigma_x - \tau \frac{B_x(B_x + B_y)}{\pi}\sigma_y - \frac{1}{4}B_x B_y(\Delta t - \tau)\sigma_z. \tag{3.11}$$

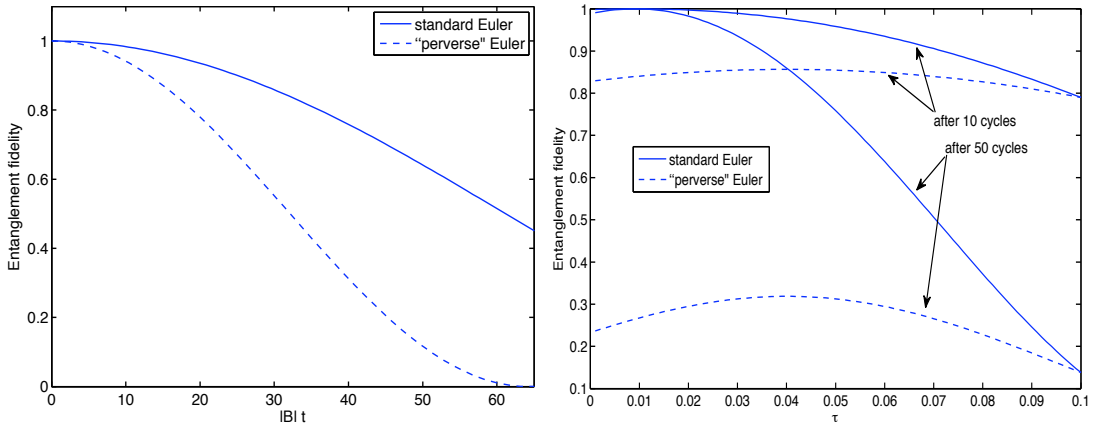

(a) F_e vs. time with $\tau = 0.05 = \Delta t/2$

(b) F_e at fixed time vs. τ with $\Delta t = 0.1$.

Figure 3.5: Standard and "perverse" Euler sequences.

A comparison of the peformance of these two sequences is shown in Figure 3.5(a), and their dependence on τ in Figure 3.5(b). The standard Euler sequence produces better results, as one might expect, and interestingly its $\bar{H}_0^{(1)}$ does not depend on Δt. Sequences based on other Eulerian

cycles–for example, the alternative XYYXYXXY mentioned earlier–which use the standard pulse placement are found to have an $\bar{H}_0^{(1)}$ which is identical to Eq. (3.10) except that the terms may have different signs, and all show identical behavior. From now on when we refer to the Euler sequence, we refer to the standard pulse placement, at the end of each Δt interval.

Finally, an example of the improvement from using the Euler sequence XYXYYXYX with the standard pulse placement versus the naive sequence $XYXY$ is shown in Figure 3.6. Here we see F_e vs. time with a fixed value of Δt for two different values of τ, one which is so small as to approach the BB limit, and one for which $\tau = \Delta t/2$. The performance of the naive XYXY sequence declines quite dramatically with this increase in τ; the peformance of the Euler sequence hardly changes over the same scale.

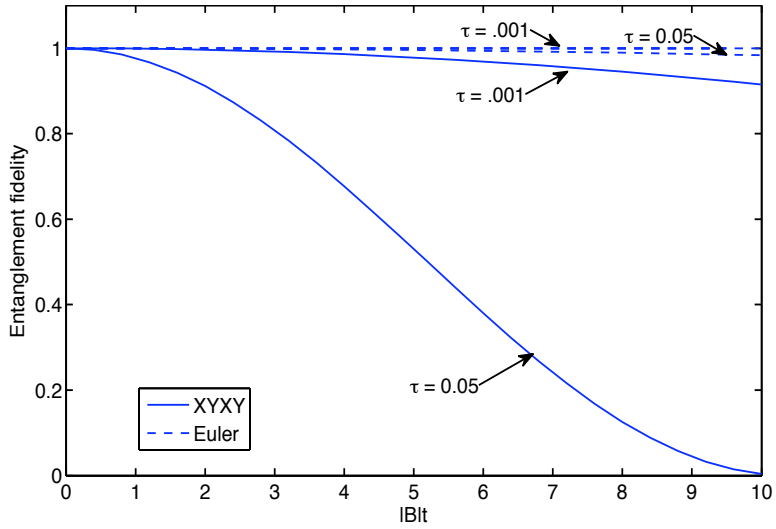

Figure 3.6: 4-pulse XYXY sequence (dashed lines) and 8-pulse XYXYYXYX Euler sequence (solid lines) for $\tau = 0.01, ..., 0.1$.

A more rigorous test of the efficacy of the Euler sequence is offered by considering T_{999} for a wide range of Δt and τ values for both the XYXY and Euler sequences. The 3D plot of T_{999} vs. Δt and τ for the Euler sequence is shown in Figure 3.7, which is analogous to Figure 3.3 for the XYXY sequence. Taking the array of T_{999} values from these two plots and subtracting the XYXY values from the Euler values yields a difference which is never negative; thus, for all values of Δt and τ we have observed, and possibly for all values, using the Euler sequence quite simply will keep the entanglement fidelity above a threshold longer. For moderately long times, as in Figure 3.8(a), the performance of the XYXY sequence may approach that of the Euler for $\tau = \tau_{max}$, although the

robustness of the Euler sequence with respect to τ is also apparent here; taking advantage of the high performance of the XYXY sequence at τ_{max} would manifestly require much finer tuning of the parameters Δt and τ than simply using the Euler sequence. Furthermore, Figure 3.8(b) shows that even at τ_{max} the Euler sequence keeps F_e above the threshold for a time which is several orders of magnitude longer.

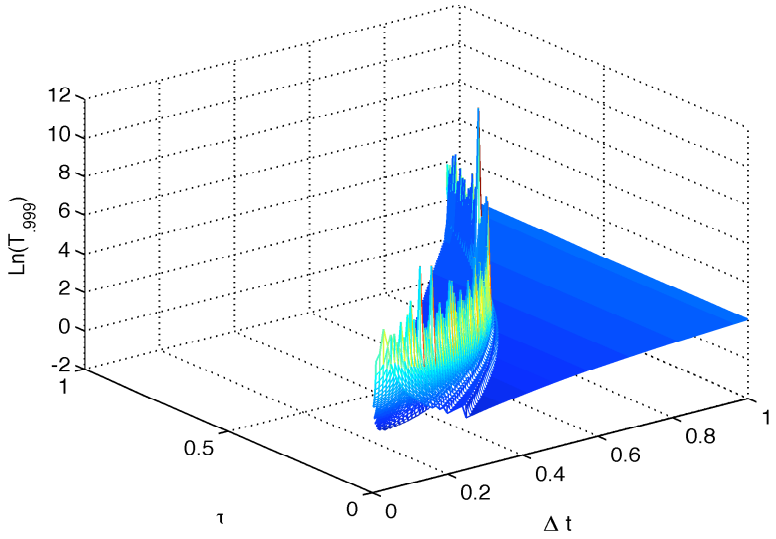

Figure 3.7: Time for entanglement fidelity to drop below a threshold of .999 for 8-pulse XYXYYXYX Euler sequence vs. Δt and τ.

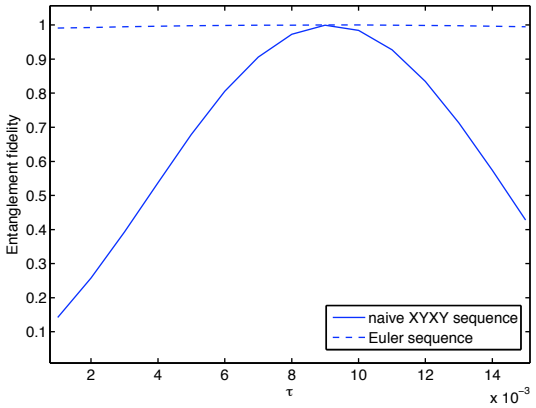

(a) Entanglement fidelity at a fixed time $|B|t = 40$ vs. τ for 4-pulse XYXY sequence (solid line) and 8-pulse XYXYYXYX Euler sequence (dashed line). For the optimal value of τ, the peformance of the XYXY sequence approaches that of the Euler, but never exceeds it. The Euler sequence is significantly more robust to the change in τ.

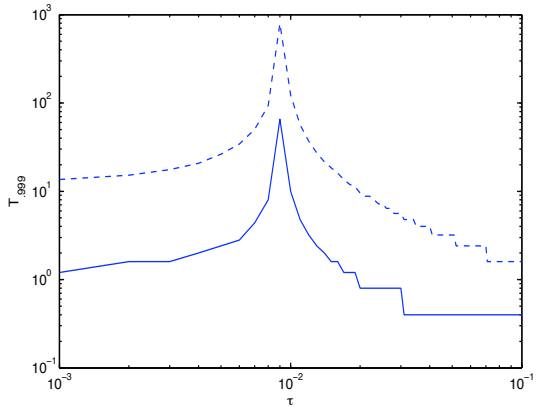

(b) $T_{.999}$ for 4-pulse XYXY sequence (solid line) and 8-pulse XYXYYXYX Euler sequence (dashed line). For moderately long times, as in Figure 3.8(a), the performance of the XYXY sequence can approach that of the Euler at τ_{max}, but here we see that the Euler sequence keeps F_e above the threshold for a time which is several orders of magnitude greater.

Figure 3.8: Naive XYXY sequence and Euler sequence.

3.3 Second-order decoupling

What about $\bar{H}_0^{(1)}$? As already mentioned, it is known for the case of bang-bang sequences that a control propagator which is time-symmetric about the center of the cycle—that is, $U_c(t) = U_c(T_c - t)$, where T_c is the cycle time—will cancel $\bar{H}_0^{(1)}$ and all other odd-order terms in the average Hamiltonian. In the BB case, we know we must maintain the XYXY structure in order to preserve the cancellation of $\bar{H}_0^{(0)}$, but we can achieve time symmetry by following the XYXY sequence with its mirror image YXYX, in which pulses take place at the beginning of each Δt interval rather than the end. This gives us a sequence XYXYYXYX; however, the two Y pulses in the middle of the cycle correspond to a full rotation, which has no net effect on the qubit, so we can leave them out. Thus, an appropriate bang-bang sequence for canceling $\bar{H}_0^{(0)}$ and $\bar{H}_0^{(1)}$ is the 6-pulse sequence XYXXYX, still of length $8\Delta t$, where the two middle X pulses are separated by $2\Delta t$.

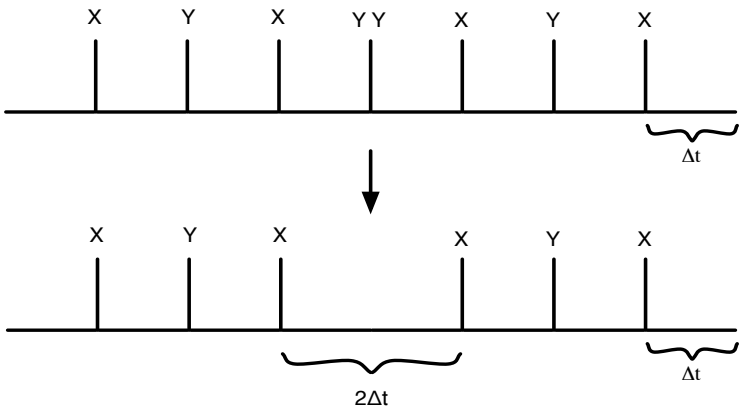

Indeed, this pulse sequence dramatically increases the effectiveness of the decoupling relative to the XYXY sequence, as can be seen in Figure 3.9(a), where F_e vs. time is plotted for a few different values of Δt. Figure 3.9(b) offers a more comprehensive comparison, with $T_{.999}$ vs. Δt for both sequences, in which we see that $T_{.999} \propto \Delta t^{-2}$ for the symmetrized BB (SBB) sequence, compared to $T_{.999} \propto \Delta t^{-2}$ for the regular XYXY BB sequence. This is similar to the τ dependence for the CP and symmetrized CP sequences in the previous chapter.

In order to cancel $\bar{H}_0^{(1)}$ with finite pulses, we use our intuition from the bang-bang case that time-symmetrizing the control suceeds in canceling odd-ordered terms, as in the symmetrized Carr-Purcell sequence examined previously. That this works for arbitrary bounded-strength DD has not yet been formally proven, but the fact that it works in the cases examined strongly supports general

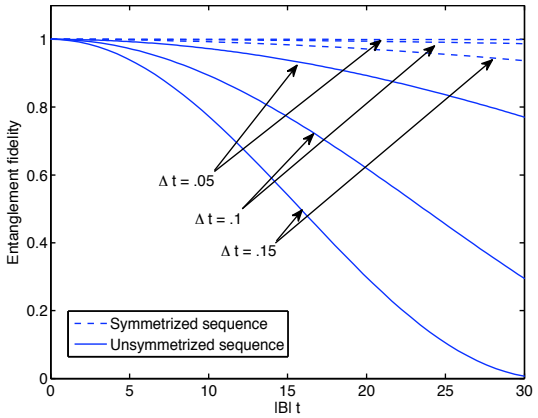

(a) Bang-bang control using 4-pulse XYXY sequence (solid line) and 6-pulse XYXXYX symmetrized sequence (dashed line) for $\Delta t = 0.05, 0.1, 0.15$.

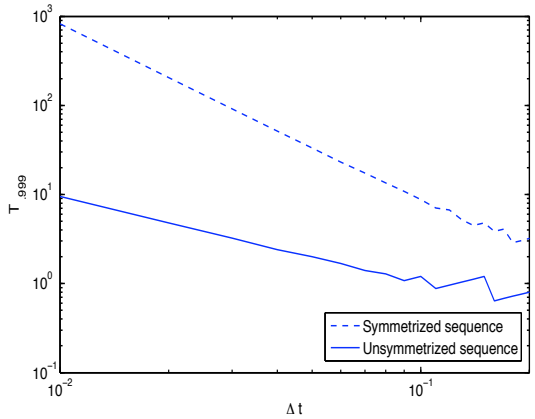

(b) $T_{.999}$ vs. Δt with bang-bang control using 4-pulse XYXY sequence (solid line) and 6-pulse XYXXYX symmetrized sequence (dashed line)

Figure 3.9: 4-pulse XYXY sequence and 6-pulse XYXXYX symmetrized sequence

applicability. In the bang-bang case, because the pulses happen instantaneously, time symmetry can be achieved simply by mirroring the 4-pulse XYXY sequence to yield the 6-pulse sequence described above; with finite pulses, however, the way in which the pulses themselves are implemented becomes important. As we saw for the Euler supercycle in the case of the known magnetic field, we can time-symmetrize the 8-pulse Eulerian sequence in this more general case by doubling the length and performing the second half "in reverse," with opposite phases for the propagators which realize the pulses. In the case where $\tau < \Delta t$, this means that the pulses in the second half of the cycle take place at the beginning of the Δt. This sequence will be known as the Euler supercycle, and its effect compared to the standard Euler sequence is shown in Figure 3.10(a) for a few representative values of τ, where we see that the performance gained in using the Euler supercycle versus the standard Euler is as great as that gained by using the Euler sequence versus the naive XYXY sequence.

An overview of the performance of the Euler supercycle is given in Figure 3.11, which shows the $T_{.999}$ versus Δt and τ. This picture differs significantly from that of the naive XYXY sequence or the standard first-order Euler sequence, in that the "ridge" of high-performing values of Δt and τ is absent, and in general the best-performing values are small Δt and τ. In Figure 3.12(a) and Figure 3.12(b) we see that for a range of τ values around τ_{max} the original Euler sequence outperforms the supercycle, presumably because of cancellation among higher order terms, as we saw with the XYXY sequence. However, we expect that in a more realistic open-system setting, this cancellation would not occur, meaning that the supercycle would have an advantage for all values of τ. Even in this

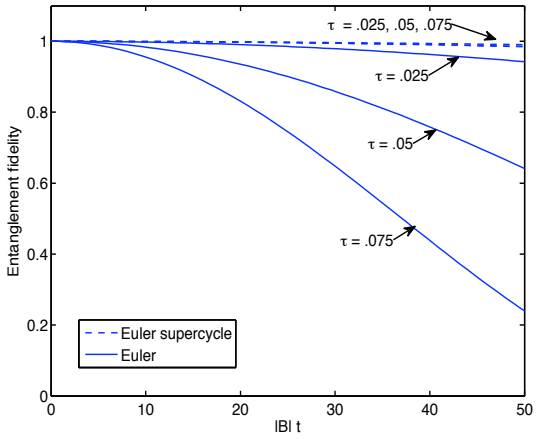

(a) Entanglement fidelity vs. time for Euler and Euler supercycle with a few different values of τ for $\Delta t = .1$.

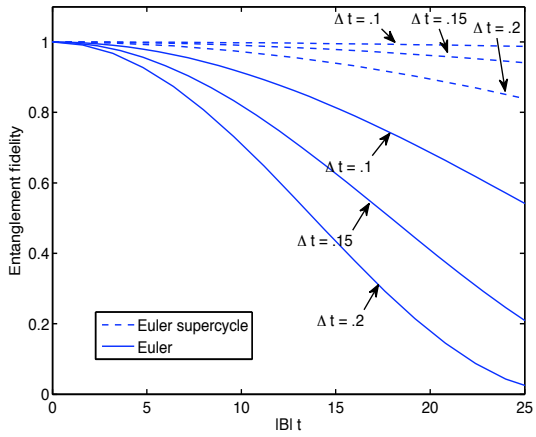

(b) Entanglement fidelity vs. time for Euler and Euler supercycle with a few different values of Δt for $\tau = \Delta t$.

Figure 3.10: Comparison between symmetrized and unsymmetrized Euler sequences.

simple setting, for larger τ the advantage of the standard Euler is quickly lost, and the supercycle proves to be extraordinarily robust to changes in τ in general.

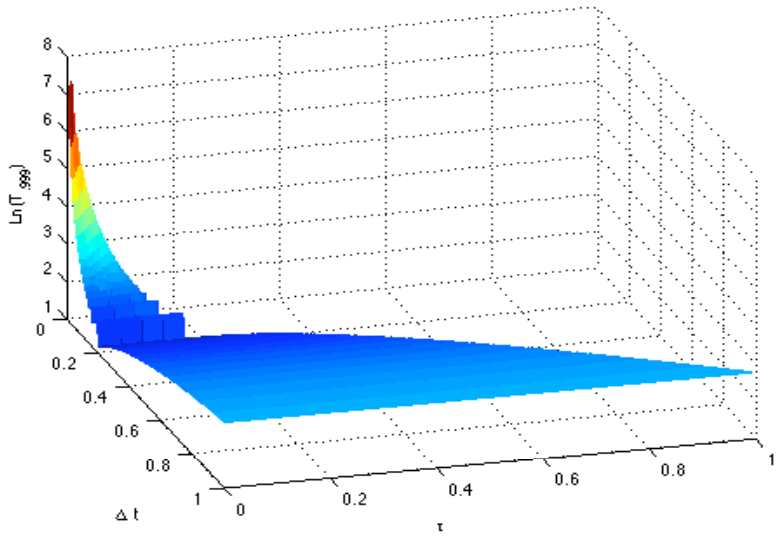

Figure 3.11: Time for entanglement fidelity to drop below a threshold of .999 vs. Δt and τ for Euler supercycle (symmetrized Euler).

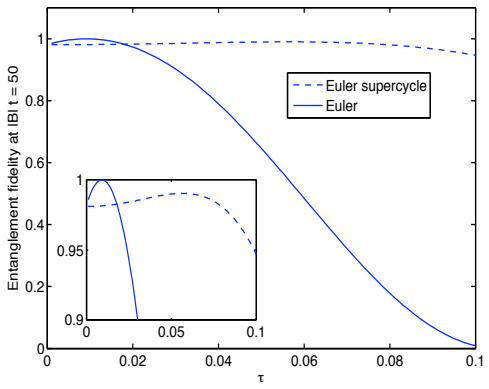

(a) Entanglement fidelity at fixed time $|B|t = 50$ vs. τ for Euler and Euler supercycle. For a certain range of τ, the Euler actually outperforms the symmetrized version, although this advantage is quickly lost as τ increases. The inset shows a closeup of the high-F_e region, in which we have a better view of the nonmonotonic dependence of the supercycle performance on τ and the extent to which it is outperformed by the standard Euler for $\tau < 0.02$.

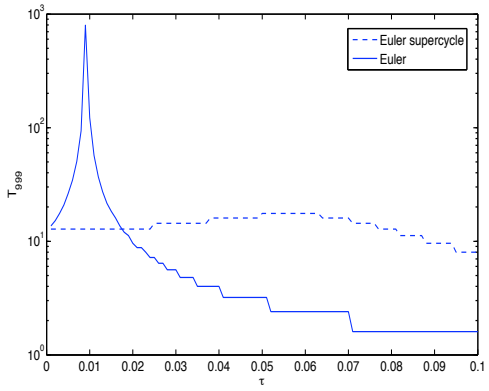

(b) Time for entanglement fidelity to drop below a threshold of .999 vs. τ for Euler and Euler supercycle, with $\Delta t = .1$ For the right value of τ the Euler dramatically outperforms the supercycle, although for large τ the Euler supercycle is better.

Figure 3.12: Comparison between symmetrized and unsymmetrized Euler sequences.

Chapter 4

Fault Tolerance Properties

4.1 Problem Setting

Thus far the control we have been considering, even where the pulses have width, has been "perfect" in the sense that each pulse realizes exactly the intended rotation. However, as mentioned in the introduction, the other major obstacle in realizing quantum information processing, besides decoherence, is error which arises from the control itself. Strategies such as fault-tolerant quantum error correction [59], [60], [54], encoding via exchange interactions [53], and concatenated dynamical decoupling [57] attempt to overcome this obstacle. The Eulerian method has the advantage of naturally maintaining $\bar{H}_0^{(0)} = 0$ with systematic control errors; in this spirit, here we consider the effects of imperfections in the implementation of the control, to investigate predictions that the Eulerian method will prove more robust than BB schemes. For simplicity, we limit ourselves to two kinds of systematic error: parallel, in which the control has an error in the same direction as the original pulse, and perpendicular, in which the error occurs in an orthogonal direction, so that an X pulse, for example, will have a small perturbation in Y. Parallel error may be thought of as error in the rotation angle, while perpendicular error corresponds to error in the rotation axis. For the case of BB control, this means that the propagator describing an X pulse with parallel error becomes, for example,

$$P_x = \exp\{-i\pi\sigma_x/2\} \rightarrow P_x^{'} = \exp\{-i(\pi + \epsilon_{\|})\sigma_x/2\} \tag{4.1}$$

or for perpendicular error

$$P_x^{'} = \exp\{-i(\pi\sigma_x/2 + \epsilon_\perp \sigma_y/2)\}. \tag{4.2}$$

For finite pulses we can place the error explicitly in the control Hamiltonian, which becomes

$$H_c = \frac{\pi}{\tau}\frac{\sigma_x}{2} \rightarrow H_c^{'} = \frac{\pi}{\tau}\frac{\sigma_x}{2} + \frac{\epsilon_\parallel}{\tau}\frac{\sigma_x}{2} \tag{4.3}$$

in the case of parallel error and

$$H_c^{'} = \frac{\pi}{\tau}\frac{\sigma_x}{2} \rightarrow \frac{\pi}{\tau}\frac{\sigma_x}{2} + \frac{\epsilon_\perp}{\tau}\frac{\sigma_y}{2}. \tag{4.4}$$

in the case of perpendicular error.

Following [**?**], however, we will not take the control propagator implementing the rotation as $U_c(s) = \exp\{-iH_c^{'}s\}$ for the purposes of calculating terms in $\bar{H}$; instead, it is convenient to go into the logical frame with perfect control, as before, and to group the error term in the Hamiltonian with H_0. So, for example, the control propagator for the 8-pulse Euler sequence with $\tau = \Delta t$ is still:

$$U_c(t) = \begin{cases} \exp\{-i(\pi/\tau)(\sigma_x/2)s\} \cdot \mathbb{I} & 0 \leq t < \Delta t \quad s \in [0,\tau] \\ \exp\{-i(\pi/\tau)(\sigma_y/2)s\} \cdot \sigma_x & 2\Delta t \leq t < 2\Delta t \quad s \in [0,\tau] \\ \exp\{-i(\pi/\tau)(\sigma_x/2)s\} \cdot \sigma_z & 3\Delta t \leq t < 3\Delta t \quad s \in [0,\tau] \\ \exp\{-i(\pi/\tau)(\sigma_y/2)s\} \cdot \sigma_y & 4\Delta t \leq t < 4\Delta t \quad s \in [0,\tau] \\ \exp\{-i(\pi/\tau)(\sigma_y/2)s\} \cdot \mathbb{I} & 5\Delta t \leq t < 5\Delta t \quad s \in [0,\tau] \\ \exp\{-i(\pi/\tau)(\sigma_x/2)s\} \cdot \sigma_y & 6\Delta t \leq t < 6\Delta t \quad s \in [0,\tau] \\ \exp\{-i(\pi/\tau)(\sigma_y/2)s\} \cdot \sigma_z & 7\Delta t \leq t < 7\Delta t \quad s \in [0,\tau] \\ \exp\{-i(\pi/\tau)(\sigma_x/2)s\} \cdot \sigma_x & 8\Delta t \leq t < 8\Delta t \quad s \in [0,\tau] \end{cases}$$

while the new H_0 is given by

$$H_0^{'}(t) = \begin{cases} H_0 + \frac{\epsilon}{\tau}\frac{\sigma_i}{2} & 0 \leq \quad t \quad < \Delta t \quad s \in [0,\tau] \\ H_0 + \frac{\epsilon}{\tau}\frac{\sigma_j}{2} & 2\Delta t \leq \quad t \quad < 2\Delta t \quad s \in [0,\tau] \\ H_0 + \frac{\epsilon}{\tau}\frac{\sigma_i}{2} & 3\Delta t \leq \quad t \quad < 3\Delta t \quad s \in [0,\tau] \\ H_0 + \frac{\epsilon}{\tau}\frac{\sigma_j}{2} & 4\Delta t \leq \quad t \quad < 4\Delta t \quad s \in [0,\tau] \\ H_0 + \frac{\epsilon}{\tau}\frac{\sigma_j}{2} & 5\Delta t \leq \quad t \quad < 5\Delta t \quad s \in [0,\tau] \\ H_0 + \frac{\epsilon}{\tau}\frac{\sigma_i}{2} & 6\Delta t \leq \quad t \quad < 6\Delta t \quad s \in [0,\tau] \\ H_0 + \frac{\epsilon}{\tau}\frac{\sigma_j}{2} & 7\Delta t \leq \quad t \quad < 7\Delta t \quad s \in [0,\tau] \\ H_0 + \frac{\epsilon}{\tau}\frac{\sigma_i}{2} & 8\Delta t \leq \quad t \quad < 8\Delta t \quad s \in [0,\tau] \end{cases}$$

where $i, j = x, y$ if the errors are parallel, and vice versa if they are perpendicular, and $H_0 = \vec{B} \cdot \vec{\sigma}$. We have already seen that in the absence of errors this sequence cancels $\bar{H}_0^{(0)}$; a feature of the Euler sequence is that the contribution to $\bar{H}_0^{(0)}$ from *both* types of errors is also canceled:

$$\begin{aligned} \bar{H}^{(0)}_{0_{error}} &= \frac{\epsilon}{2\tau}\int_0^\tau \Big\{ \mathbb{I}\, u_x^\dagger(t)\sigma_i u_x(t)\, \mathbb{I} + \sigma_x\, u_y^\dagger(t)\sigma_j u_y(t)\, \sigma_x + \sigma_z\, u_x^\dagger(t)\sigma_i u_x(t)\, \sigma_z + \sigma_y\, u_y^\dagger(t)\sigma_j u_y(t)\, \sigma_y \\ &\qquad + \mathbb{I}\, u_y^\dagger(t)\sigma_j u_y(t)\, \mathbb{I} + \sigma_y\, u_x^\dagger(t)\sigma_i u_x(t)\, \sigma_y + \sigma_z\, u_y^\dagger(t)\sigma_j u_y(t)\, \sigma_z + \sigma_x\, u_x^\dagger(t)\sigma_i u_x(t)\, \sigma_x \Big\}\, dt \\ &= 0. \end{aligned}$$

That the Euler sequence is fault-tolerant to lowest order against the types of errors considered here is the basis for statements that it has enhanced robustness. We will see below how errors affect $\bar{H}_0^{(1)}$, and how the actual evolution under each sequences fares in numerical simulation.

4.2 Parallel Errors

4.2.1 Naive XYXY sequence

Interestingly, we can see that the first four terms in the integral in (4.5), which correspond to the naive transcription of the XYXY sequence with finite pulses, are equal to zero independently of the second four terms in the case of parallel errors. That is, although the XYXY sequence still has a nonzero $\bar{H}_0^{(0)}$, recalled below in Eq. (4.5), it also succeeds at cancelling the lowest-order contribution

from parallel errors, so $\bar{H}_0^{(0)}$ is no different than in the ideal case. Looking at $\bar{H}_0^{(0)}$ and $\bar{H}_0^{(1)}$ for the XYXY sequence with errors is instructive because, as with ideal control, the terms are both nonzero, meaning that we can look at their competition to understand some of the more surprising behavior. Specifically, recall that the "ridge" of high-performing Δt and τ occured at values that caused $\bar{H}_0^{(0)}$ and $\bar{H}_0^{(1)}$ to cancel each other. This intuition is preserved in the case of control with errors; again we find that the full expression for $\bar{H}_0^{(1)}$ is complicated, but much insight can be gained by looking at just the dominant terms, which are linear in Δt or $\epsilon_\parallel$ and are the contributions from the periods of free evolution. As noted above, with parallel errors $\bar{H}_0^{(0)}$ for the XYXY sequence remains the same as with perfect control:

$$\bar{H}_0^{(0)} = -\frac{B_x + B_y}{\pi}\frac{\tau}{\Delta t}\sigma_z \tag{4.5}$$

while $\bar{H}_0^{(1)}$ picks up a term proportional to $\epsilon_\parallel$:

$$\bar{H}_0^{(1)} \approx \left[B_x B_y \Delta t + \frac{B_x + B_y}{2}\epsilon_\parallel\right]\sigma_z \tag{4.6}$$

Now these terms will be equal in magnitude and will cancel each other when

$$\tau \approx \frac{\pi}{2}\epsilon_\parallel \Delta t + \frac{B_x B_y}{B_x + B_y}\pi \Delta t^2. \tag{4.7}$$

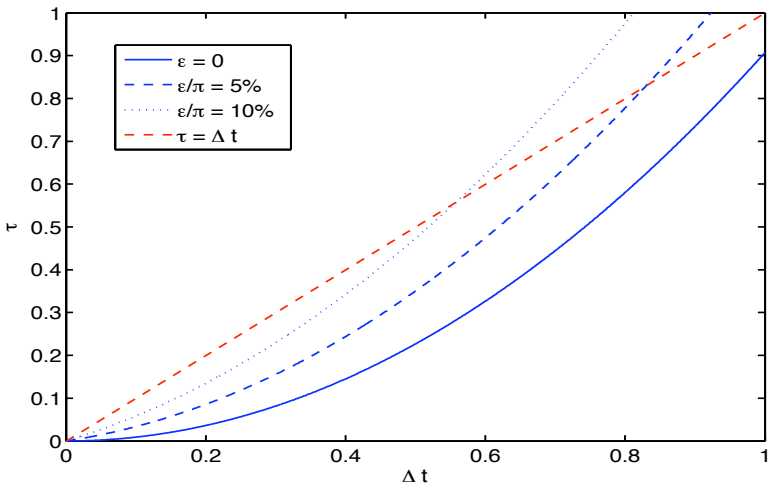

Figure 4.1: τ values from (4.7) for different values of $\epsilon_\parallel$, indicating the expected behavior of the high-performing ridge of values with increasing parallel error.

Figure 4.1 shows this value of τ vs. Δt for a few different values of $\epsilon_\parallel$. Thus, in looking at the

performance of the naive XYXY sequence we should still see the ridge of best-performing values, but now in a different location for each different value of $\epsilon_{\|}$, and indeed this expectation is correct. Figure 4.3 shows an overhead view of a series of plots of the kind seen in Figure 3.3; $T_{.999}$ vs. Δt and τ for different values of $\epsilon_{\|}$, up to an error of 10% (that is, $\epsilon_{\|}/\pi = 10\%$). The τ value which gives the maximum performance for each Δt for the various $\epsilon_{\|}$ values is shown in Figure 4.2, illustrating the progression of the ridge as $\epsilon_{\|}$ increases.

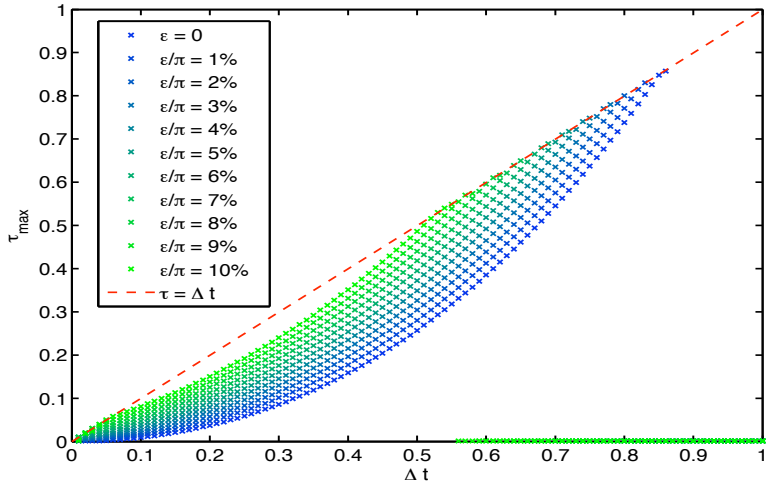

Figure 4.2: Value of τ which produces maximum performance for each Δt, for various values of $\epsilon_{\|}$. The same plot holds for both the XYXY and the 8-pulse Euler sequence.

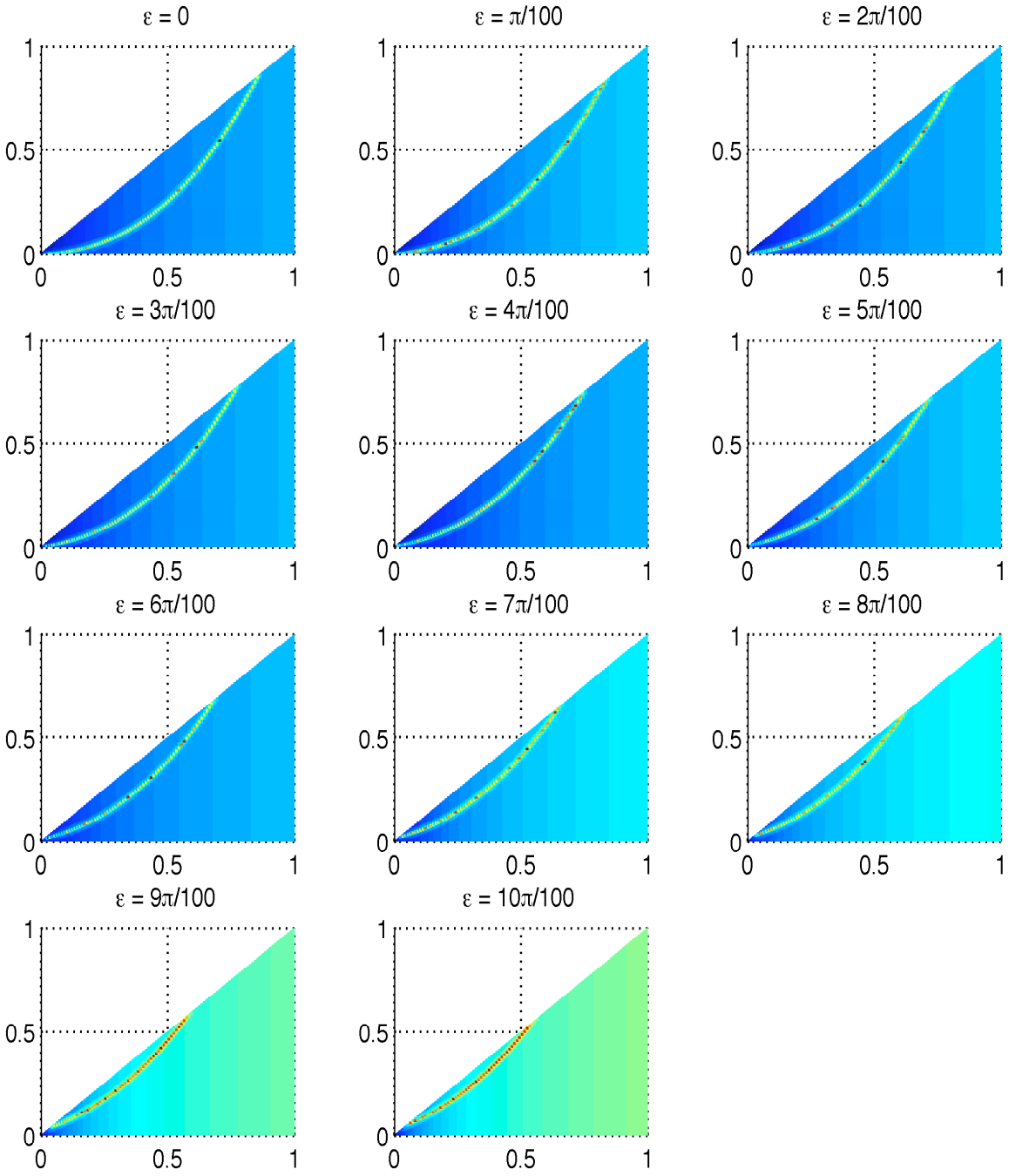

Figure 4.3: XYXY sequence with finite pulses: overhead view of 3D plots, showing the time for the entanglement fidelity to drop below .999 as a function of Δt and τ, for different values of parallel errors. Color is proportional to height along the z-axis. Note how the "ridge" of best Δt and τ values shifts with increasing error.

Understanding how the position of the ridge changes with $\epsilon_{\|}$ is important because the dependence

of the performance on $\epsilon_\parallel$ at any given $(\Delta t, \tau)$ point is determined by how the ridge moves in relation to it. That is, increasing $\epsilon_\parallel$ does not necessarily lead to decreased performance for the system under consideration. For points such that the ridge moves closer with increasing $\epsilon_\parallel$, for example, the performance will increase monotonically with $\epsilon_\parallel$; points where the ridge "passes over" will show a nonmonotonic dependence. It is unlikely that this unusual behavior would be reproduced if the environment were modeled in a more realistic fashion, causing the dynamics to become irreversible, but for our simple system it is impossible to ignore it, so heavily does it dominate the dependence on $\epsilon_\parallel$ for this sequence. Figure 4.4 shows how $T_{.75}$ depends on $\epsilon_\parallel$ at several different $(\Delta t, \tau)$ points. The addition of $\epsilon_\parallel$ as a parameter complicates visualization of the space; for simplicity, here we consider only the case where $\tau = \Delta t$, since ultimately we are interested in the behavior of these sequences at the low-power limit.

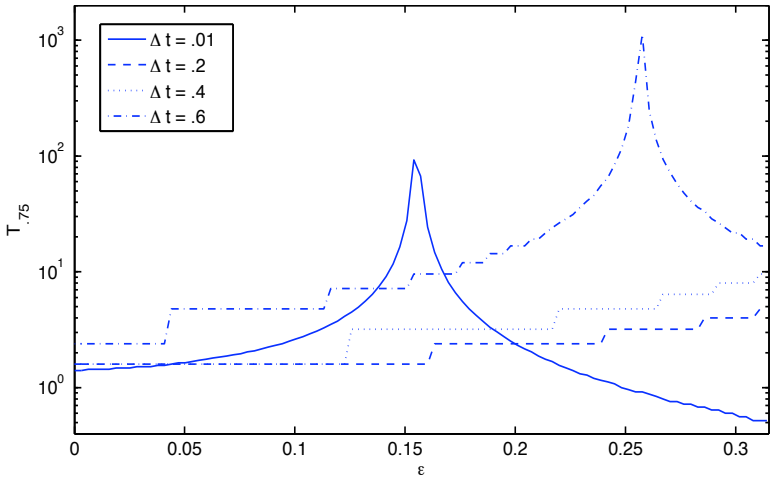

Figure 4.4: $T_{.75}$ vs. $\epsilon_\parallel$ for XYXY sequence with parallel error, with $\tau = \Delta t$.

For $\Delta t = 0.2$ and $\Delta t = 0.4$ we see a monotonic increase in performance as $\epsilon_\parallel$ increases; from Figure 4.1 we see the endpoints of the ridge move inward and approach these points with increasing $\epsilon_\parallel$. The performance at the other two points, $\Delta t = 0.01$ and $\Delta t = 0.6$, shows a nonmonotonic dependence on $\epsilon_\parallel$, with the peak performance occuring at the value of $\epsilon_\parallel$ for which the ridge passes over the point, as seen again in Figure 4.1.

4.2.2 Euler sequence

We have seen above that the Euler sequence still has $\bar{H}_0^{(0)} = 0$ for parallel error. An $\epsilon_\parallel$ dependence does, however, appear in $\bar{H}_0^{(1)}$. Furthermore, one of the interesting properties of the Euler sequence without error is that $\bar{H}_0^{(1)}$ does not depend on Δt; with parallel errors we see that in addition to $\epsilon_\parallel$, $\bar{H}_0^{(1)}$ picks up a Δt dependence:

$$\bar{H}_0^{(1)} = -\frac{(2B_y\Delta t + \epsilon_\parallel)(B_x + B_y)}{2\pi}\left(\frac{\tau}{\Delta t}\right)\sigma_x - \frac{(2B_x\Delta t + \epsilon_\parallel)(B_x + B_y)}{2\pi}\left(\frac{\tau}{\Delta t}\right)\sigma_y. \tag{4.8}$$

Unlike the naive XYXY sequence, which has both $\bar{H}_0^{(0)}$ and $\bar{H}_0^{(1)}$ nonzero, for the Euler sequence we only have one nonzero term available, since $\bar{H}_0^{(0)} = 0$. Thus, we cannot repeat the consideration used above to find the value of τ for which the first two terms cancel; in this case, $\bar{H}_0^{(1)}$ and $\bar{H}_0^{(2)}$. Our conjecture, however, is that they cancel each other in a similar way, based on the fact that the ridge of high-performing Δt and τ values for the Euler sequence occurs in exactly the same location as for the naive XYXY sequence for all values of $\epsilon_\parallel$ we have observed. The Euler sequence is different, however, in that for every combination of parameters Δt, τ, $\epsilon_\parallel$ we have observed–for example, all the values in Figure 4.3–the Euler sequence has superior performance; not suprisingly, since it has $\bar{H}_0^{(0)} = 0$. The analogous figure for the Euler sequence is Figure 4.5, which again shows $T_{.999}$ vs. Δt and τ for different values of $\epsilon_\parallel$ with color corresponding to height along the z-axis. The similarity to Figure 4.3 in the placement of the ridge is clear. In fact, because the ridge is in precisely the same location as for the XYXY sequence, one can again look at Figure 4.2 for a summary. Besides the apparently universal superiority in performance, the Euler sequence also displays a feature not seen in the XYXY sequence; namely, improvement in performance as $\epsilon_\parallel$ goes to zero for small Δt, even though the ridge is moving away in this case.

Figure 4.6 shows how $T_{.75}$ varies with $\epsilon_\parallel$ for several values of Δt, with $\tau = \Delta t$. For each Δt, the dependence on $\epsilon_\parallel$ is similar to that of the XYXY sequence in Figure 4.4, except that the absolute value of $T_{.75}$ for the Euler sequence is higher; the two sequences will be compared explicitly below, in Figure 4.9. In addition, the feature mentioned above—improvement in performance as $\epsilon_\parallel$ goes to zero for small Δt, even though the ridge is moving away–is evident for $\Delta t = .01$, in contrast to the other values of Δt. With the exception of this feature, the dependence on $\epsilon_\parallel$ for each Δt can again be understood by looking at where each $(\Delta t, \tau)$ is located in relation to the ridge for each value of $\epsilon_\parallel$.

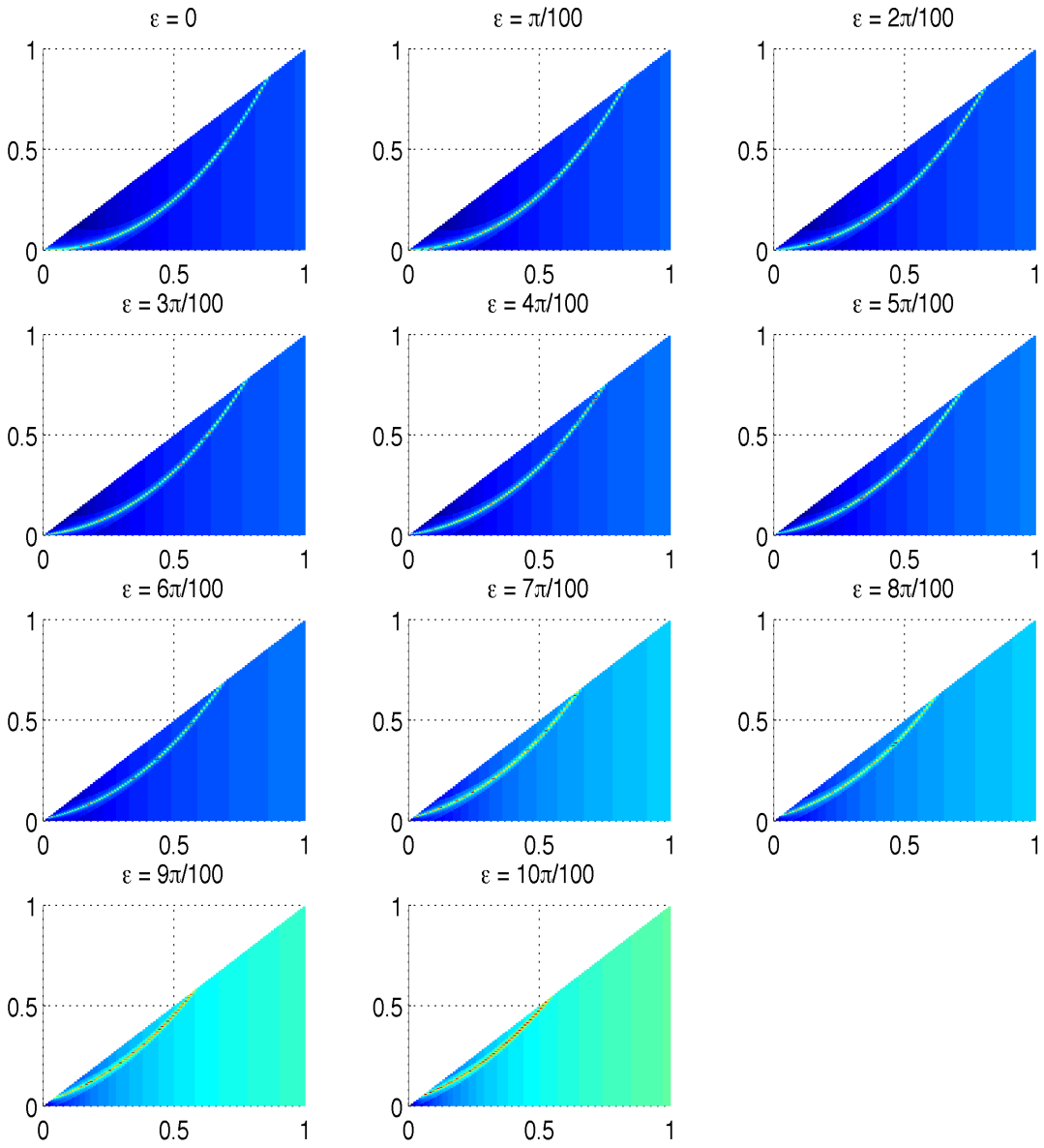

Figure 4.5: Euler sequence: overhead view of 3D plots, showing the time for the entanglement fidelity to drop below .999 as a function of Δt and τ, for different values of parallel errors. Color is proportional to height along the z-axis. Note how the "ridge" of best Δt and τ values shifts with increasing error.

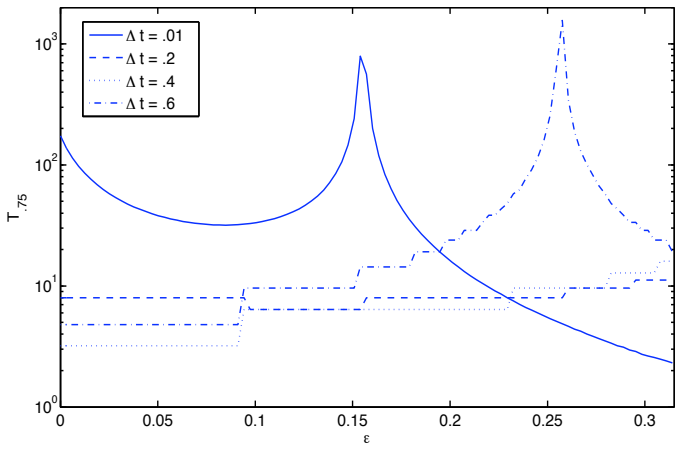

Figure 4.6: Euler sequence $T_{.75}$ vs. $\epsilon_{\|}$ for $\Delta t = 0.01, 0.2, 0.4, 0.6$, with $\tau = \Delta t$.

4.2.3 Euler supercycle

For the same reason that the Euler sequence still cancels $\bar{H}_0^{(0)}$ with error–namely, that the error can be taken to be a part of H_0 and then the structure of the Euler cycle guarantees $\bar{H}_0^{(0)} = 0$–the Euler supercycle still has both $\bar{H}_0^{(0)} = 0$ and $\bar{H}_0^{(1)} = 0$ with both kinds of error. Thus, we cannot say much analytically about what kind of behavior to expect when error is added, except that the performance of this sequence should be superior. A sequence of 3D plots showing overhead views of $T_{.999}$ vs. Δt and τ for different values of $\epsilon_{\|}$ is given in Figure 4.8. One of the distinctive features of the performance space of the supercycle without errors was the absence of a ridge of the kind seen in the XYXY or Euler sequences, but it is interesting here to note that one appears with increasing $\epsilon_{\|}$.

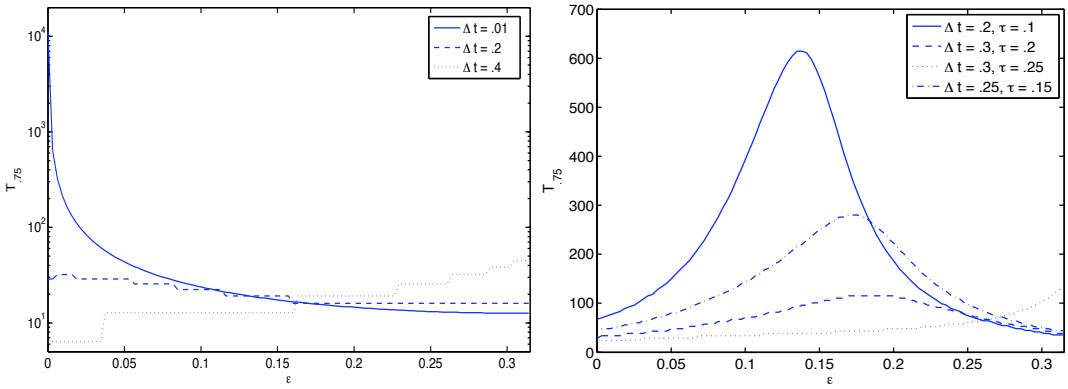

(a) $\tau = \Delta t$

(b) Various τ (see legend).

Figure 4.7: $T_{.75}$ vs. $\epsilon_{\|}$ for Euler supercycle with parallel error.

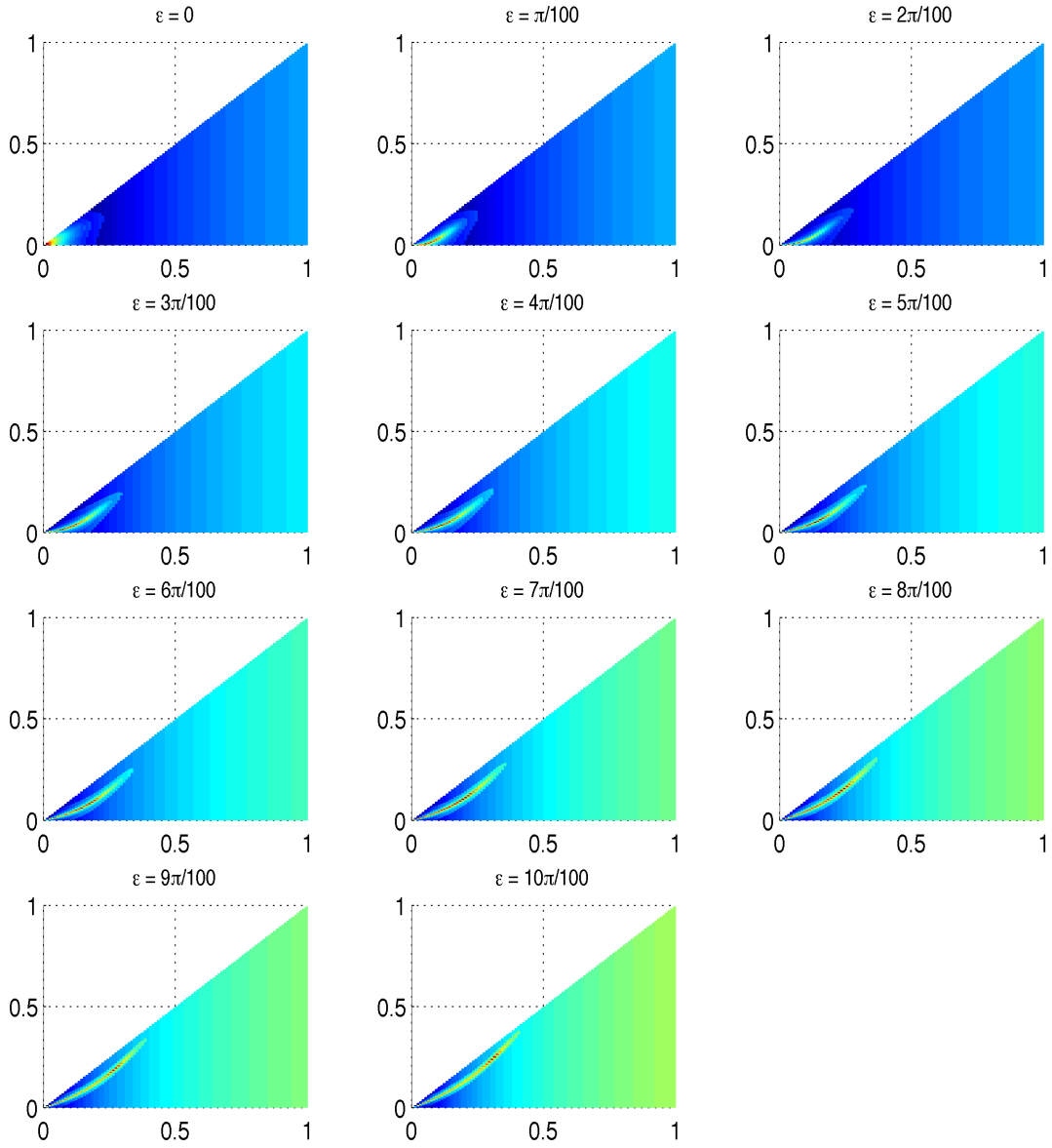

Figure 4.8: Euler supercycle: overhead view of 3D plots, showing the time for the entanglement fidelity to drop below .999 as a function of Δt and τ, for different values of parallel errors. Color is proportional to height along the z-axis. Note how a "ridge" of best Δt and τ appears with increasing error.

Figure 4.7(a) shows $T_{.75}$ vs. $\epsilon_{\|}$ for several values of Δt, with $\tau = \Delta t$, analogously to Figure 4.4 for the XYXY sequence and Figure 4.6 for the Euler. Here we see none of the nonmonotonic

behavior of the other two sequences along the $\tau = \Delta t$ line; for contrast, Figure 4.7(b) shows $T_{.75}$ vs. $\epsilon_{\|}$ for several points with $\tau < \Delta t$ which the ridge passes over as $\epsilon_{\|}$ is varied. From this it is evident that the ridge which forms as $\epsilon_{\|}$ increases is not as sharply peaked as that of the XYXY and Euler sequences.

4.2.4 Comparison

Figure 4.9 shows an explicit comparison of $T_{.75}$ vs. $\epsilon_{\|}$ for all the sequences, at three different values of Δt. For completeness, the BB XYXY sequence ($\tau = 0$) and symmetrized version (SBB) are also included. The performance space of each sequence is complicated enough, as we have seen, that these three Δt values cannot give a conclusive picture in themselves, but they do serve as illustrations of behavior which has been seen consistently over more extensive testing. First of all, as mentioned above, the Euler and XYXY sequences show a similar dependence on $\epsilon_{\|}$, but for the same values of the parameters Δt, τ, and $\epsilon_{\|}$, the Euler sequence always has a higher value of $T_{.75}$, or any T_{value}. The supercycle, surprisingly, does not always have $T_{.75}$ greater than that of the Euler cycle, or even the naive XYXY sequence; however, we see that the only Δt, τ, $\epsilon_{\|}$ points where the latter two sequences outperform the supercycle is for those on the ridge—that is, points where the lowest two nonzero terms in the average Hamiltonian conveniently cancel each other. At every other point the supercyle offers superior performance. Furthermore, in the presence of realistic environment it is unlikely that this cancellation would occur.

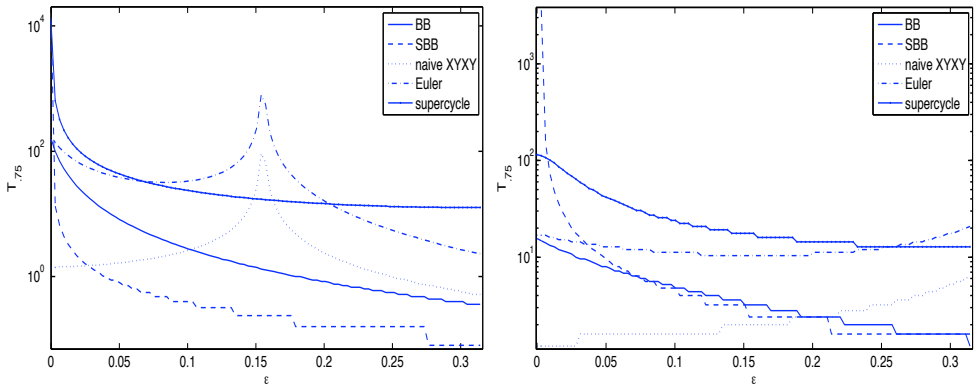

(a) $\Delta t = 0.01$ (b) $\Delta t = 0.1$

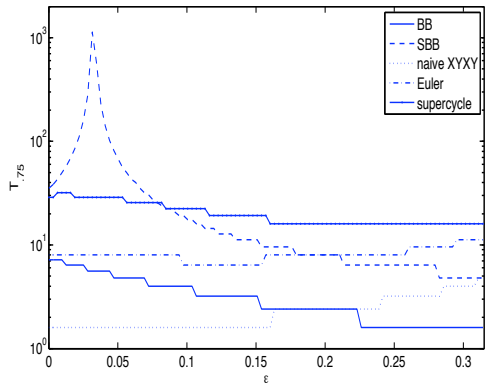

(c) $\Delta t = 0.2$

Figure 4.9: $T_{.75}$ vs. $\epsilon_{\|}$ for all sequences with parallel error, with $\Delta t = 0.01, 0.1, 0.2$.

4.3 Perpendicular error

4.3.1 XYXY sequence

In the case of perpendicular error, or rotation-axis error, we find that the naive XYXY sequence no longer cancels the additional contribution from the error Hamiltonians–see the first four terms in (4.5), now with $i = y$ and $j = x$–and instead, in contrast to Eq. (4.5), the full $\bar{H}_0^{(0)}$ is given by

$$\bar{H}_0^{(0)} = -\frac{(B_x + B_y) + \epsilon_\perp}{\pi \Delta t}\sigma_z. \tag{4.9}$$

The $\bar{H}_0^{(1)}$ term for this sequence also picks up an $\epsilon_\perp$ dependence, but unlike with parallel error we find here that there are no additional terms which are only first-order in one of Δt, τ, or $\epsilon_\perp$, so that the dominant term remains the same as with perfect control:

$$\bar{H}_0^{(1)} \approx B_x B_y \Delta t \sigma_z. \tag{4.10}$$

These will cancel one another when τ has a value of

$$\tau \approx \frac{\pi B_x B_y \Delta t^2 - \epsilon_\perp}{B_x + B_y}. \tag{4.11}$$

This value of τ is plotted vs. Δt for a few different values of $\epsilon_\perp$ in Figure 4.10. Again, the general picture is confirmed by numerical simulation of the full evolution. Figure 4.11 shows the value of τ which produces the highest $T_{.999}$ for each Δt, summarizing the results of Figure 4.12, which shows overhead views of the 3D plots for each value of $\epsilon_\perp$.

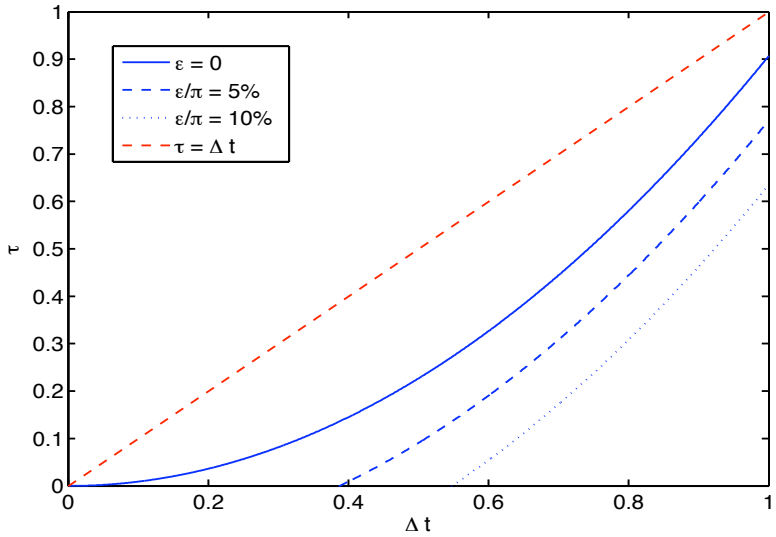

Figure 4.10: τ values from (4.11) for different values of $\epsilon_\perp$, indicating the expected behavior of the high-performing ridge of values with increasing perpendicular error.

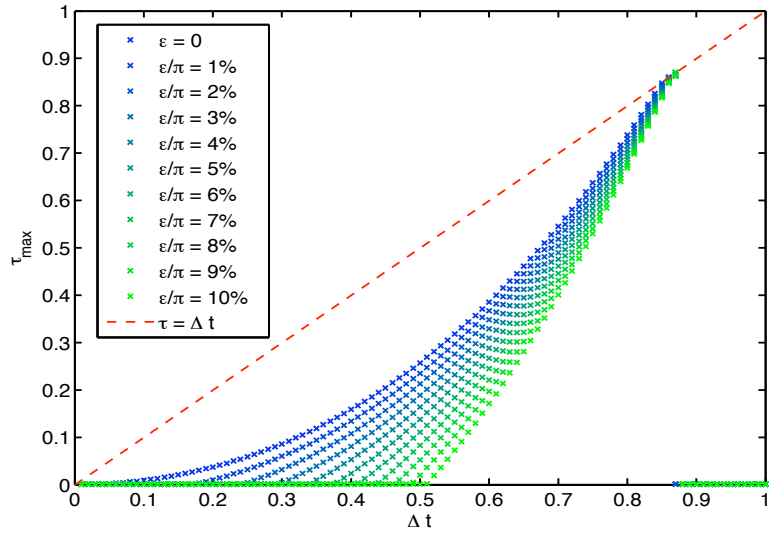

Figure 4.11: Value of τ which produces maximum performance (T_{value}) for each Δt, for various values of $\epsilon_\perp$. The same plot holds for both the XYXY and Euler sequences.

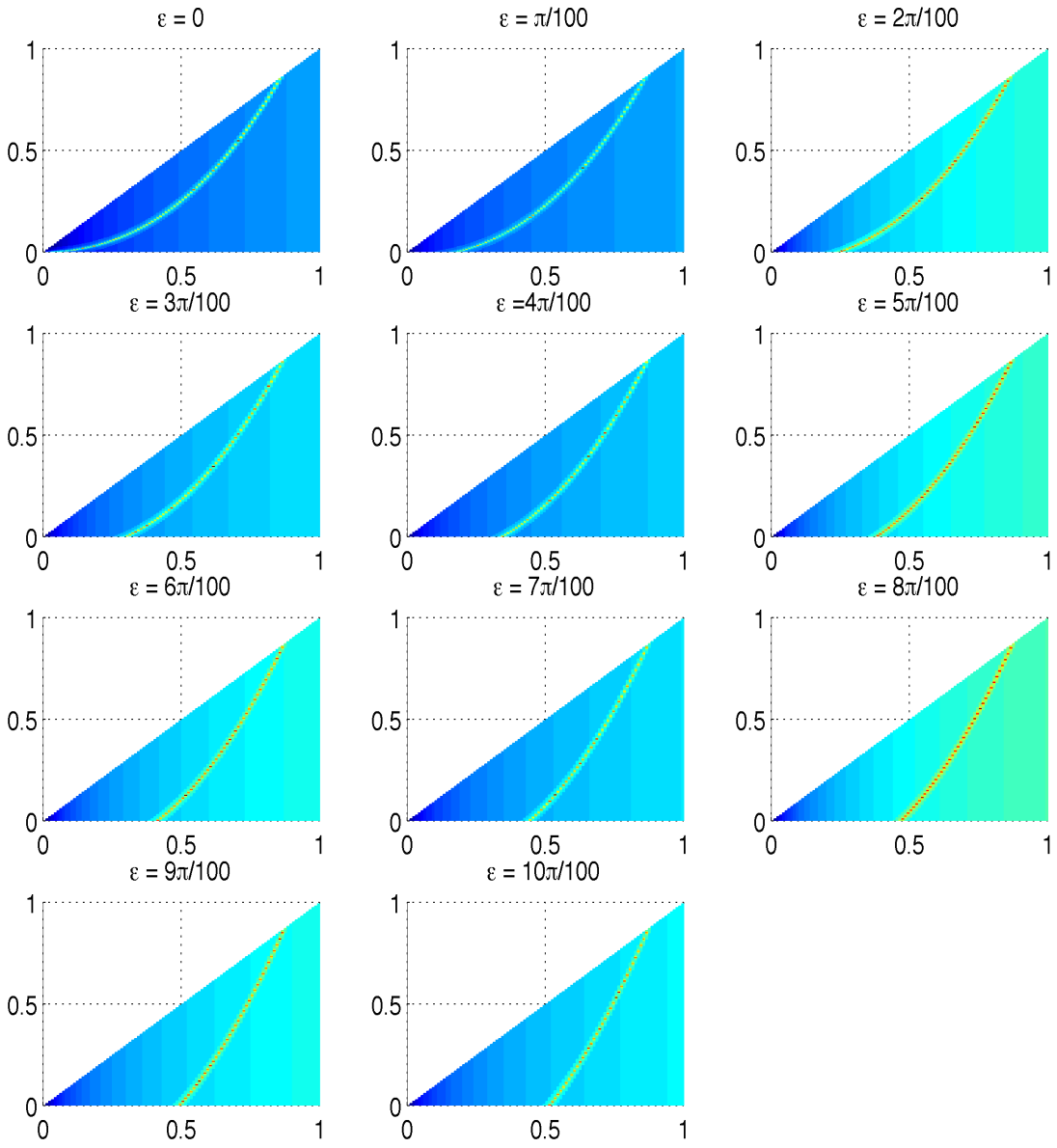

Figure 4.12: XYXY sequence with perpendicular error: overhead view of 3D plots, showing $T_{.999}$ as a function of Δt and τ, for different values of $\epsilon_\perp$. Color is proportional to height along the z-axis. Note how the "ridge" of best Δt and τ values shifts with increasing error.

As usual, Figure 4.13(a) shows $T_{.75}$ vs. $\epsilon_\perp$ for several different values of Δt, with $\tau = \Delta t$, which can be understood by considering how the ridge moves with increasing $\epsilon_\perp$ relative to each point.

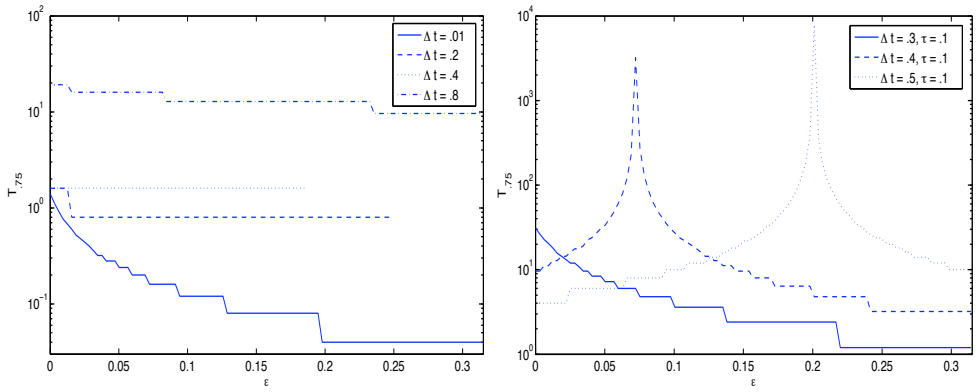

(a) $\tau = \Delta t$ (b) $\tau = 0.1$

Figure 4.13: $T_{.75}$ vs. $\epsilon_\perp$ for naive XYXY sequence with perpendicular error.

Since the ridge does not actually pass over any of these points, Figure 4.13(b) shows $T_{.75}$ vs. $\epsilon_\perp$ for several different values of Δt, with $\tau = 0.1$.

4.3.2 Euler sequence

For the Euler sequence with perpendicular error, we find that unlike the case of parallel error, $\bar{H}_0^{(1)}$ picks up an $\epsilon_\perp$ dependence, but not a Δt dependence:

$$\bar{H}_0^{(1)} = \frac{-B_y\left[(B_x + B_y)\tau + \epsilon_\perp\right]}{\pi}\sigma_x - \frac{-B_x\left[(B_x + B_y)\tau + \epsilon_\perp\right]}{\pi}\sigma_y. \tag{4.12}$$

As with parallel error, in the results of numerical simulations we see here that the value of τ which produces the best results for a given Δt is identical to that of the naive XYXY sequence. The sequence of 3D plots showing the progression of the ridge is given in Figure 4.14. As always, even though the dependence on Δt and τ is very similar to the naive sequence, the Euler is found to have superior performance. The value of $T_{.75}$ vs. $\epsilon_\perp$ for a few values of Δt is shown in Figure 4.15(a) with $\tau = \Delta t$, and in Figure 4.15(b) for $\tau = .1$.

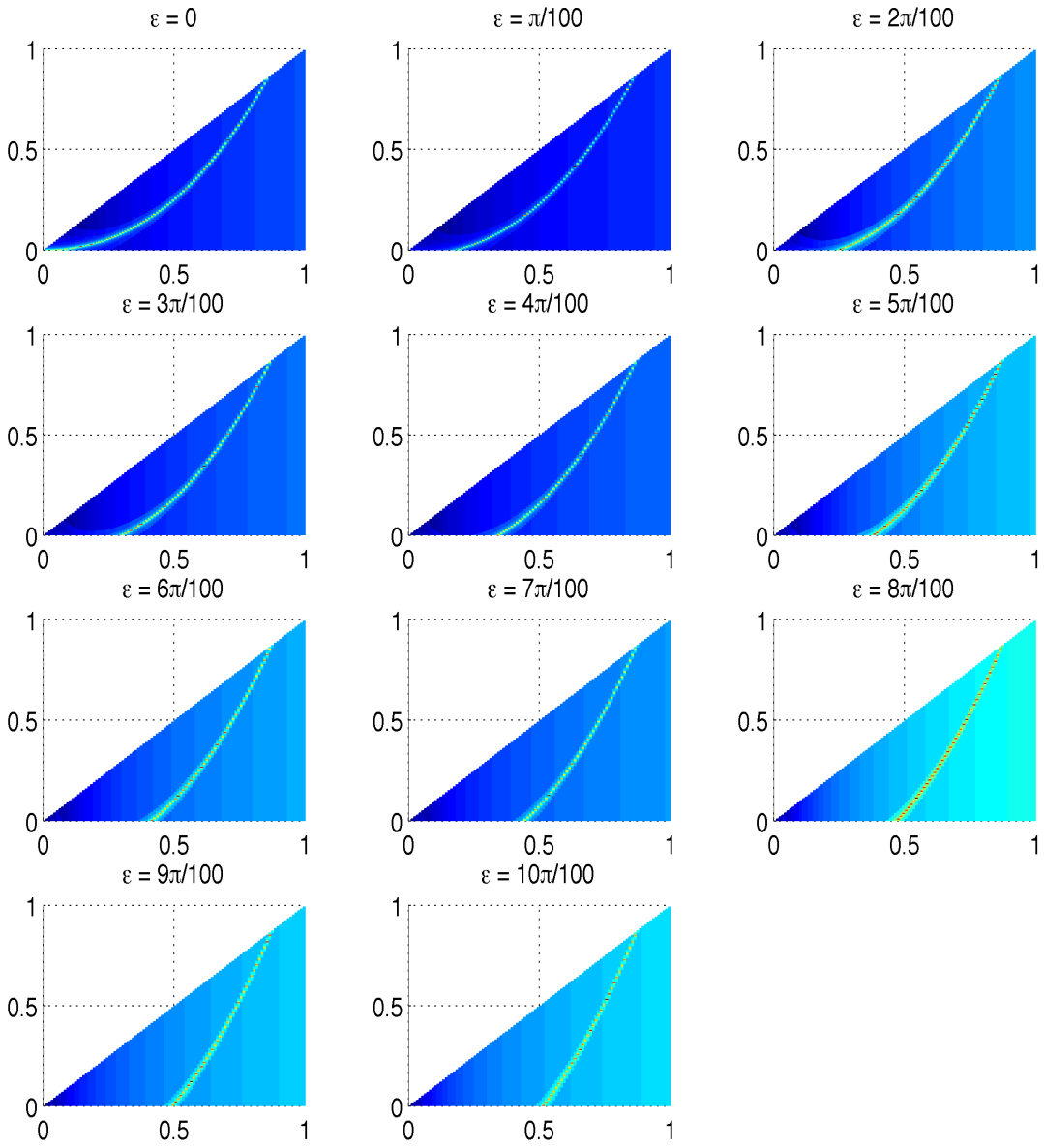

Figure 4.14: Euler sequence: overhead view of 3D plots, showing the time for the entanglement fidelity to drop below .999 as a function of Δt and τ, for different values of the perpendicular error. Color is proportional to height along the z-axis. Note how the "ridge" of best Δt and τ values shifts with increasing error.

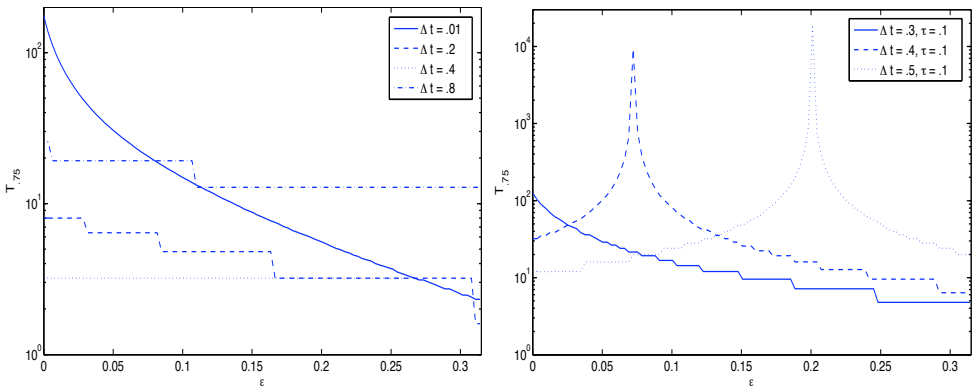

(a) $\tau = \Delta t$ (b) $\tau = 0.1$

Figure 4.15: $T_{.75}$ vs. $\epsilon_\perp$ for Euler sequence with perpendicular error.

4.3.3 Euler supercycle

As mentioned above, the Euler supercycle maintains $\bar{H}_0^{(0)} = 0$ and $\bar{H}_0^{(1)} = 0$ with perpendicular error as well, so only a phenomenological analysis of the effect of error is available. The usual series of 3D plots showing $T_{.75}$ vs. Δt and τ for different values of $\epsilon_\perp$ is given in Figure 4.17. A small ridge appears with increasing ϵ and moves in the direction of increasing Δt. Figure 4.16(a) shows $T_{.75}$ vs. $\epsilon_\perp$ for a few values of Δt, with $\tau = \Delta t$; to display the profile of the ridge which forms, Figure 4.16(b) shows $T_{.75}$ vs. $\epsilon_\perp$ for a few values of Δt, with $\tau = 0.1$.

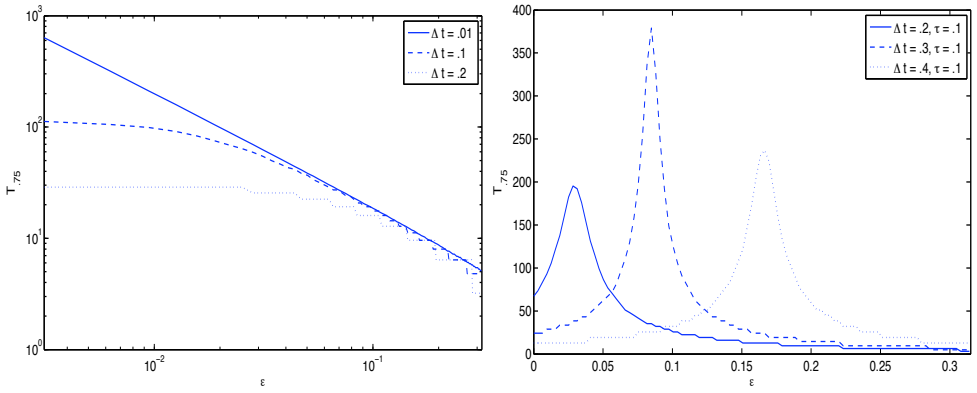

(a) $\tau = \Delta t$ (b) $\tau = 0.1$

Figure 4.16: $T_{.75}$ vs. $\epsilon_\perp$ for Euler supercycle with perpendicular error.

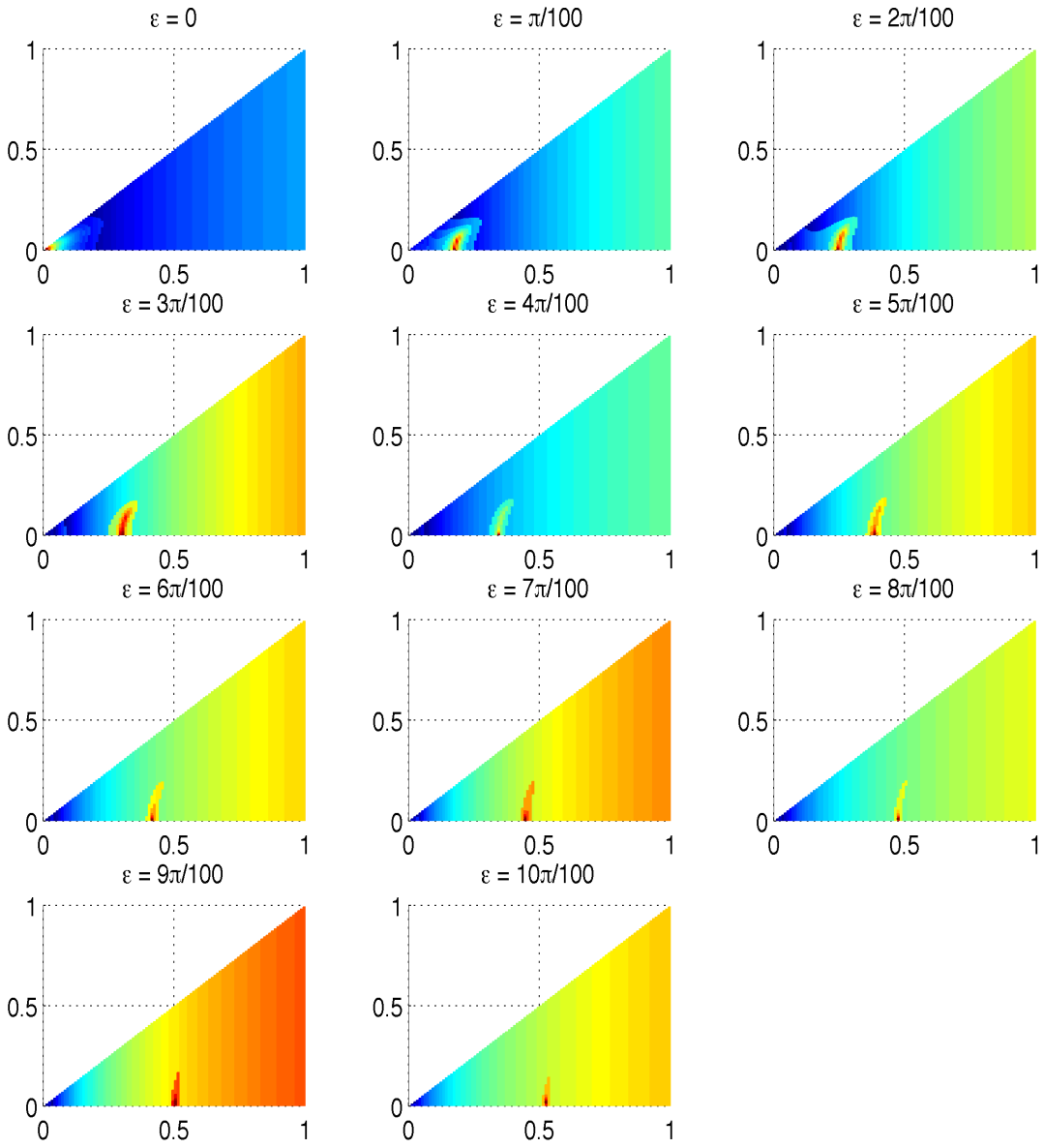

Figure 4.17: Euler supercycle: overhead view of 3D plots, showing $T_{.999}$ as a function of Δt and τ, for different values of the perpendicular error. Color is proportional to height along the z-axis. Note how the "ridge" of best Δt and τ values shifts with increasing error.

4.3.4 Comparison

Like Figure 4.9 for parallel error, Figure 4.3.4 shows an explicit comparison of $T_{.75}$ vs. $\epsilon_\perp$ for all the sequences, at the same three different values of Δt. In 4.18(a), the absence of nonmonotonic behavior allows a more straightforward comparison of the sequences, with the Euler supercycle again dominant. In 4.18(b) and 4.18(c), the general statements we can make are the same as for the case of parallel errors in Figure 4.9: the Euler sequence always outperforms the naive XYXY sequence for the same parameters, period, and the Euler supercycle outperforms all other sequences except at points where Δt, τ, and $\epsilon_\perp$ are such that the leading terms in the average Hamiltonian for those sequences conveniently cancel each other; i.e., on the ridge. It is also evident that the same can be said of the Euler sequence with $\tau = \Delta t$ and the BB XYXY sequence ($\tau = 0$); that the Euler outperforms even the BB except for at the peak performance of the latter. In both cases, the continued existence of the peaks in a more realistic open-system scenario is doubtful, so we might expect that the Euler sequence, for example, would outperform the XYXY sequence with any value of τ more generally.

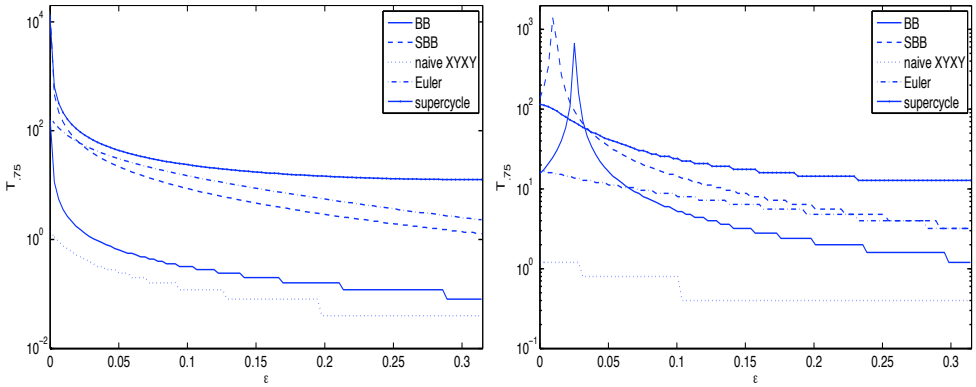

(a) $\Delta t = 0.01$ (b) $\Delta t = 0.1$

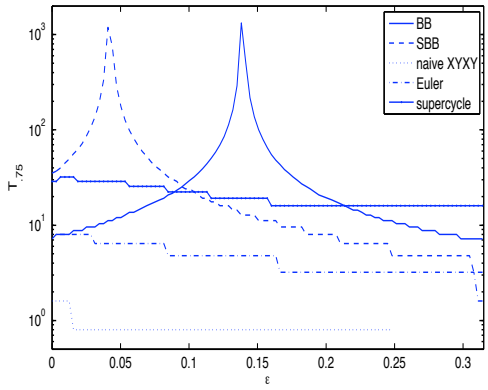

(c) $\Delta t = 0.2$

Figure 4.18: $T_{.75}$ vs. $\epsilon_\perp$ for all sequences with perpendicular error, with $\Delta t = 0.01, 0.1, 0.2$.

Chapter 5

Conclusions

5.1 Summary of results

We have reviewed the original work on both bang-bang and Eulerian dynamical decoupling, and investigated the performance of each in a simple but instructive control setting, considering both the limit of low-power control and the effect of two types of systematic errors in control implementation. In the case of known single-qubit dynamics, we demonstrated the impact of finite-width effects, showing that for the XX Carr-Purcell sequence $\bar{H}_0^{(0)} \neq 0$ when $\tau \neq 0$ and that the entanglement fidelity decays more quickly with increasing τ, as $T_{.999} \propto \tau^{-1}$. We also saw that the time-symmetrized "++−" sequence, which has both $\bar{H}_0^{(0)} = 0$ and $\bar{H}_0^{(1)} = 0$, does indeed produce superior performance; although $T_{.999}$ drops more quickly, as $T_{.999} \propto \tau^{-2}$, the absolute value of F_e is always greater than for the unsymmetrized sequence. The performance of both sequences depends more weakly on Δt; increasing Δt with τ fixed causes $T_{.999}$ to decay quickly to a non-zero asymptotic value determined by τ.

For the unknown single-qubit dynamics, we have observed that, similar to the sequences above, the symmetrized BB sequence offers performance superior to the unsymmetrized XYXY sequence, even though $T_{.999} \propto \Delta t^{-2}$ for the symmetrized sequence and $T_{.999} \propto \Delta t^{-1}$ for the unsymmetrized. We also saw that the XYXY sequence, intended for use with BB pulses, is strongly affected by increasing the pulse width τ, and does quite poorly in the low-power limit. The 8-pulse Euler sequence, designed to work with bounded-strength control, provides universally better performance, as predicted by average Hamiltonian theory. It is not possible to obtain a simple relationship between

$T_{.999}$ and τ of Δt for these sequences, because the dependence is dominated by the existence of optimal $(\Delta t, \tau)$ combinations which cause the first two non-zero terms in the average Hamiltonian to cancel each other, leading to a sharp peak in $T_{.999}$. The 16-pulse Euler supercycle emerges as an even more promising option than the Euler cycle; it performs better than both the naive XYXY and standard Euler sequences except at the convenient $(\Delta t, \tau)$ values of the latter, and is significantly more robust to changes in τ.

With error we find again that the Euler sequence is universally better than the naive XYXY with the same parameters and in some cases outperforms even the XYXY with BB pulses. The Euler supercycle is extraordinarily robust to error, cancelling both $\bar{H}_0^{(0)}$ and $\bar{H}_0^{(1)}$ with both types of error considered, and offering superior performance over even the BB and SBB sequences except at the error values where the latter sequences have coincidentally high performance. Evaluating the claims that the Euler sequence is more robust to error is problematic with this system because of the existence of the high-performing "ridge" of $(\Delta t, \tau)$ values, which shifts location with increasing ϵ. Since increasing the error at many $(\Delta t, \tau)$ points actually improves performance for these sequences, a discussion of robustness may not even be meaningful; nevertheless, it should be noted that the Euler supercycle is manifestly more robust than either the XYXY or standard Euler.

In a more realistic control scenario, we expect that the more "coincidental" features—the sharp peaks in $T_{.999}$ where cancellation between terms occurs—would not be observed, but that the relative performance of the sequences under consideration and their general dependence on Δt and τ would remain intact.

5.2 Outlook

A natural next step, which is already underway, is to try the Euler and Euler supercycle sequences in a more realistic open-system setting; for example, by placing the qubit in contact with a spin bath. Wenxian Zhang has performed some tests of these sequences in a quantum-dot model, taking into account the hyperfine interaction, and preliminary results are encouraging and seem to confirm the main results obtained here. It would also, of course, be exciting to implement these sequences in an experimental setting. Combining the Eulerian method with another decoherence control method, exploring additional symmetries, or considering explicitly time-dependent control Hamiltonians could also be fruitful pursuits with the goal of cancelling higher orders in the average Hamiltonian or further increasing the fault-tolerance of the Eulerian sequences.

Bibliography

[1] H. P. Breuer and F. Petruccione, *The Theory of Open Quantum Systems* (New York: Oxford University Press, 2002).

[2] F. Benatti and R. Floreanini, eds., *Irreversible Quantum Dynamics* (Heidelberg: Springer-Verlag, 2003).

[3] U. Weiss, *Quantum Dissipative Systems* (Singapore: World Scientific, 1993).

[4] D. P. Vincenzo, Science **270** 255 (1995).

[5] A. M. Steane, Rep. Prog. Phys. **61**, 117 (1998).

[6] M. A. Nielsen and I. L. Chuang, *Quantum Computation and Quantum Information* (Cambridge University Press, Cambridge, UK, 2000).

[7] O. Hirota, A. S. Holevo, and C. M. Caves, *Quantum Communication, Computing, and Measurement* (New York: Plenum Press, 1997).

[8] M. Palma, K. -A. Suominen, and A. K. Ekert, Proc. R. Soc. London, Ser. A **452**, 567 (1996).

[9] D. J. Wineland *et al.*, Proc. R. Soc. London Ser. A **454**, 411 (1998).

[10] F. De Martini, G. Denardo, and Y. Shih, *Quantum Interferometry* (Berlin: VCH Publishing Group, 1996).

[11] U. Haeberlen, *High Resolution NMR in Solids: Selective Averaging* (Academic Press, New York, 1976).

[12] R. R. Ernst, G. Bodenhausen, and A. Wokaun, *Principles of Nuclear Magnetic Resonance in One and Two Dimensions* (Oxford University Press, Oxford, 1994).

[13] P. W. Brumer and M. Shapiro, *Principles of the Quantum Control of Molecular Processes* (New York: Wiley and Sons, 2003).

[14] M. D. LaHaye, O. Buu, B. Camarota, K. C. Schwab, Science **304**, 74 (2004).

[15] C. W. Gardiner, *Quantum Noise* (Berlin: Springer, 1991).

[16] J. F. Poyatos, J. I. Cirac, and P. Zoller, Phys. Rev. Lett. **77**, 4728 (1996).

[17] L. -M. Duan and G. -C. Guo, Phys. Rev. Lett. **79**, 1953 (1997).

[18] P. Zanardi and M. Rasetti, Phys. Rev. Lett. **79**, 3306 (1997).

[19] D. A. Lidar, I. L. Chuang, and K. B. Whaley, Phys. Rev. Lett. **81**, 2594 (1998).

[20] E. Knill, R. Laflamme, and L. Viola, Phys. Rev. Lett. **84**, 2525 (2000).

[21] A. Kitaev, Ann. Phys. **303**, 2 (2003).

[22] S. Bravy and A. Kitaev, quant-ph/9811052 (1998).

[23] P. Zanardi and S. Lloyd, Phys. Rev. Lett **90**, 067902 (2003).

[24] H. M. Wiseman, Phys. Rev. A **49**, 2133 (1994).

[25] H. M. Wiseman, Phys. Rev. A **50**, 4428 (1994).

[26] C. Ahn, H. M. Wiseman, and G. J. Milburn, Phys. Rev. A **67**, 052310 (2003).

[27] A. C. Doherty and K. Jacobs, Phys. Rev. A **60**, 2700 (1999).

[28] C. Ahn, A. C. Doherty, and A. J. Landahl, Phys. Rev. A **65**, 042301 (2002).

[29] P. W. Shor, Phys. Rev. A **52**, 2493 (1995).

[30] A. M. Steane, Phys. Rev. Lett **77**, 793 (1996).

[31] E. Knill, R. Laflamme, and W. H. Zurek, Science **279**, 342 (1998).

[32] L. Viola, "Advances in Decoherence Control," quant-ph/0404038 v1 (2004).

[33] L. Viola and S. Lloyd, "Dynamical suppression of decoherence in two-state quantum systems," Phys. Rev. A **58**, 2733 (1998).

[34] L. Viola, E. Knill, and S. Lloyd, Phys. Rev. Lett. **82**, 2417 (1999).

[35] L. Viola, E. Knill, and S. Lloyd, Phys. Rev. Lett. **83**, 4888 (1999).

[36] P. Zanardi, Phys. Lett. A **258**, 77 (1999).

[37] D. Vitali and P. Tombesi, Phys. Rev. A **59**, 4178 (1999).

[38] L. Viola, Phys. Rev. A **66**, 012307 (2002).

[39] D. A. Lidar and W. A. Wu, Phys. Rev. Lett. **88**, 017905 (2002).

[40] W. A. Wu and D. A. Lidar, Phys. Rev. Lett **88**, 207902 (2002).

[41] M. S. Byrd and D. A. Lidar, Quantum Inf. Proc. **1**, 19 (2002).

[42] L. Viola and E. Knill, "Robust Dynamical Decoupling of Quantum Systems with Bounded Controls," Phys. Rev. Lett. **90**, 037901 (2003).

[43] A. G. Butkovskiy and Yu. I. Samoilenko, *Control of Quantum Mechanical Processes and Systems* (Dordrecht: Kluwer Academic, 1990).

[44] A. Blaquiere et al., eds., *Modeling and Control of Systems in Engineering, Quantum Mechanics, Economics and Biosciences* (New York: Springer-Verlag, 1989).

[45] S. Lloyd and L. Viola, Phys. Rev. A **65**, 010101 (2002)

[46] C. Altafini, J. Math Phys. **44**, 2357 (2003).

[47] A. M. Steane, Nature (London) **399**, 124 (1999).

[48] E. L. Hahn, Phys. Rev. **80**, 580 (1950).

[49] U. Haeberlen and J. S. Waugh, Phys. Rev. **175**, 453 (1968).

[50] P. Wocjan, "Efficient decoupling schemes with bounded controls based on Eulerian orthogonal arrays," Phys. Rev. A **73**, 7 (2006).

[51] P. Chen, "Geometric continuous dynamical decoupling with bounded controls," Phys. Rev. A **73**, 022343 (2006).

[52] B. Bollobás, *Modern Graph Theory* (Springer-Verlag, New York, 1998).

[53] M. Mohseni and D. A. Lidar, Phys. Rev. Lett. **94**, 040507 (2005).

[54] A. M. Steane, "Overhead and noise threshold of fault-tolerant quantum error correction," Phys. Rev. A **68**, 042322 (2003).

[55] E. Knill, "Quantum Computing with Very Noisy Devices," quant-ph/0410199.

[56] B. M. Terhal and G. Burkard, "Fault-tolerant quantum computation for local non-Markovian noise," quant-ph/0402104.

[57] K. Khodjasteh, D. A. Lidar, "Concatenated dynamical decoupling," quant-ph/0408128.

[58] W. G. Alway, J. A. Jones, *Arbitrary precision composite pulses for NMR quantum computing*, quant-ph 0709.0602 v1 (2007)

[59] D. P. DiVincenzo and P. W. Shor, Phys. Rev. Lett. **77**, 3260 (1996).

[60] J. Preskill, Proc. R. Soc. London A **454**, 385 (1998).

[61] B. Schumacher, Phys. Rev. A **54**, 2614 (1996).

[62] E. M. Fortunato *et al.*, New J. Phys. **4**, 5 (2002).

[63] M. A. Nielsen, Phys. Lett. A **303**, 249 (2002).

[64] E. M. Fortunato, L. Viola, J. Hodges, G. Teklemariam, and D. G. Cory, New J. Phys. **4**, 5.1 (2002).

[65] H. Y. Carr and E. M. Purcell, Phys. Rev. **94**, 630 (1954)

[66] A. J. Berglund, quant-ph/0010001.

[67] E. Fraval, M. J. Sellars, J. J. Longdell, "Dynamical decoherence control of a solid-state nuclear quadrupole qubit," oai:arXiv.org:quant-ph/0412061 (2004)